

Air Force Institute of Technology

**AFIT Scholar**

---

Theses and Dissertations

Student Graduate Works

---

9-2006

## **Modeling Fracture in Z-Pinned Composite Co-Cured Laminates Using Smeared Properties and Cohesive Elements in DYNA3D**

Jason K. Freels

Follow this and additional works at: <https://scholar.afit.edu/etd>



Part of the [Aerospace Engineering Commons](#), and the [Materials Science and Engineering Commons](#)

---

### **Recommended Citation**

Freels, Jason K., "Modeling Fracture in Z-Pinned Composite Co-Cured Laminates Using Smeared Properties and Cohesive Elements in DYNA3D" (2006). *Theses and Dissertations*. 3526.  
<https://scholar.afit.edu/etd/3526>

This Thesis is brought to you for free and open access by the Student Graduate Works at AFIT Scholar. It has been accepted for inclusion in Theses and Dissertations by an authorized administrator of AFIT Scholar. For more information, please contact [richard.mansfield@afit.edu](mailto:richard.mansfield@afit.edu).



**MODELING FRACTURE IN Z-PINNED  
COMPOSITE CO-CURED LAMINATES USING  
SMEARED PROPERTIES AND COHESIVE  
ELEMENTS IN DYNA3D**

THESIS

Jason K. Freels, Captain, USAF

AFIT/GMS/ENY/06-S01

**DEPARTMENT OF THE AIR FORCE  
AIR UNIVERSITY**

***AIR FORCE INSTITUTE OF TECHNOLOGY***

---

**Wright-Patterson Air Force Base, Ohio**

APPROVED FOR PUBLIC RELEASE; DISTRIBUTION UNLIMITED

The views expressed in this thesis are those of the author and do not reflect the official policy or position of the United States Air Force, Department of Defense, or the United States Government.

AFIT/GMS/ENY/06-S01

**MODELING FRACTURE IN Z-PINNED COMPOSITE CO-CURED  
LAMINATES USING SMEARED PROPERTIES AND COHESIVE  
ELEMENTS IN DYNA3D**

THESIS

Presented to the Faculty

Department of Aeronautics and Astronautics

Graduate School of Engineering and Management

Air Force Institute of Technology

Air University

Air Education and Training Command

In Partial Fulfillment of the Requirements for the

Degree of Master of Science (Material Science)

Jason K. Freels, BS

Captain, USAF

September 2006

APPROVED FOR PUBLIC RELEASE; DISTRIBUTION UNLIMITED.

AFIT/GMS/ENY/06-S01

**MODELING FRACTURE IN Z-PINNED COMPOSITE CO-CURED  
LAMINATES USING SMEARED PROPERTIES AND COHESIVE  
ELEMENTS IN DYNA3D**

Jason K. Freels, BS  
Captain, USAF

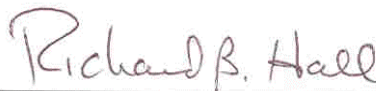
Approved:

  
\_\_\_\_\_  
Som Soni (Chairman)

5 Sep 06  
date

  
\_\_\_\_\_  
Shankar Mall (Member)

9/6/06  
date

  
\_\_\_\_\_  
Rick Hall (Member)

6 Sep 06  
date

### **Abstract**

The purpose of the present research was three-fold: 1) gain a more sophisticated understanding of the response of co-cured composite joints with and without through-thickness reinforcement (TTR), 2) compare the behavior of specimens reinforced with various sizes and densities of reinforcement, and 3) use experimental data to verify the existing DYNA3D smeared property model.

Double cantilever beam, end-notch flexure and T-section specimens reinforced with 0.011” diameter z-pins at 2% and 4% volume densities were tested to determine the mode I, mode II and mixed mode (I and II) behavior. Results were added to preliminary research in which tests were conducted on previously mentioned specimen geometries reinforced with 0.022” diameter z-pins at similar densities.

Experiments were modeled in DYNA3D using shell and cohesive elements. The energy release rate,  $G$ , determined through a curve fit developed from beam theory, was smeared across the region of reinforcement treating it as a separate material.

The research validated Z-pinning as an effective means of improving the fracture toughness of polymer matrix laminated composites in mode I and mixed mode loading conditions and determined that the existing model works well in simulating the behavior in mode I tests.

## **Acknowledgment**

I would like to express my sincere appreciation to my thesis advisor, Dr. Som Soni, as well as Dr. Hakan Kilic, Rakesh Patel and Adtech Systems Research Inc. Beavercreek, OH for the support and guidance both in the laboratory and while writing this report and for making this a great learning experience. I am truly indebted to all of you.

For helping to make materials and facilities available for the production and preparation of test specimens, I say thank you to Dr. Steven Clay, AFRL/VA and Dr. Steve Donaldson, AFRL/ML

This research project was supported, in part, by funding from AFRL/MLBC Wright Patterson AFB, OH under contract # F 33615-02-C-5008, Dr Rick Hall - Program Manager. Additional financial support was made available by NASA Glenn Research Center, Cleveland, OH under contract # NNC05AA58A, Shantaram S. Pai – Program Manager, courtesy of the hard work and generosity of the Honorable Representative from Ohio, David L. Hobson (R-07).

Finally, I cannot put into words the gratitude I have for my wife, I thank you for all the love, support, encouragement and time you have given me over the last six months, you are greatest supported and my best friend.

Jason K. Freels

# Table of Contents

	Page
Abstract .....	iv
Acknowledgements .....	v
Table of Contents .....	vi
List of Figures .....	viii
List of Tables .....	xi
I. Introduction .....	1
Scope .....	1
Motivation .....	2
Background .....	4
Z-pin Processing.....	4
DYNA3D 2000 .....	6
Research Focus.....	9
Research Objectives .....	9
II. Literature Review .....	10
Overview of Current Modeling Research.....	10
Cohesive Delamination Modeling.....	13
Cohesive Elements .....	18
III. Experimental Investigation.....	21
Overview.....	21
Test Specimen Descriptions .....	21
Un-reinforced DCB Specimens.....	21
Reinforced (Z-pinned) DCB Specimens .....	23
Reinforced and Un-reinforced ENF Specimens .....	24
Reinforced and Un-reinforced T-Section Specimens.....	25
Testing.....	29
Double Cantilever Beam (DCB) Tests.....	29
Un-reinforced DCB Tests .....	31
Reinforced (Z-Pinned) DCB Tests.....	32
Un-reinforced and Reinforced ENF Tests.....	42
Un-reinforced and Reinforced T-Section Tests.....	45



## Table of Contents (cont.)

	Page
IV. Analytical Study.....	56
DYNA3D Modeling.....	56
DCB & ENF Specimens.....	56
T-Section Specimens.....	57
Analytical/Experimental Comparisons.....	58
Un-reinforced DCB Specimens.....	58
Z-Pinned DCB Specimens.....	61
Un-reinforced ENF Specimens.....	70
Z-Pinned ENF Specimens.....	72
V. Results and Discussion.....	73
Review.....	73
Results.....	74
Effect of Z-pin Diameter and Areal Density.....	74
DCB Specimens.....	74
T-Section Specimens.....	79
Data Scatter.....	84
Performance of DYNA3D Model.....	86
Future Discussions.....	87
Conclusion.....	89
Bibliography.....	90

## List of Figures

Figure	Page
1. Insertion of Z-pins onto a Test Panel.....	5
2. Mode II Z-pin Failure Mechanisms.....	12
3. Cohesive Zone Concept.....	14
4. Bilinear Traction Displacement Model .....	15
5. DYNA3D Delamination Element Geometry .....	19
6. Unreinforced DCB Specimen Configuration.....	22
7. Z-pinned DCB Specimen Configuration .....	23
8. ENF Specimen.....	25
9. T-Specimens Dimensions and Lay-ups .....	26
10. TSA Test Set-up .....	28
11. TSA Infrared Camera Pictures .....	29
12. DCB Specimen with Crack Measurement Gage.....	30
13. Crack Locator Gage.....	30
14. Load vs. COD for Unreinforced DCB Specimens.....	31
15. CLV vs. COD for Unreinforced DCB Specimens.....	32
16. Load vs. COD for A-type Z-pinned DCB Specimens .....	33
17. CTL vs. COD for a Representative Z-pinned DCB Specimen .....	34
18. Load vs. COD for a Representative Z-pinned DCB Specimen.....	34
19. COD vs. Load/CTL (Representative DCB Specimen) .....	35
20. Load vs. COD, G-Type Z-pinned DCB Specimens.....	38
21. Load vs. COD, H-Type Z-pinned DCB Specimens.....	38
22. Load vs. COD, A-Type Z-pinned DCB Specimens.....	39
23. Load vs. COD, B-Type Z-pinned DCB Specimens.....	39

## List of Figures

Figure	Page
24. Load vs. COD, E-Type Z-pinned DCB Specimens .....	40
25. Load vs. COD, F-Type Z-pinned DCB Specimens .....	40
26. Unexpected Fracture of DCB Specimen.....	41
27. Un-reinforced ENF Test Results .....	43
28. Reinforced (Z-pinned) ENF Test Results .....	43
29. Unexpected Fracture of Z-pinned ENF Specimen.....	44
30. T-Specimen TPB Test Fixture.....	45
31. T-Specimen Strain Gage and Support Locations.....	46
32. Vishay CEA-06-125UN-350 Strain Gage .....	47
33. Load-Stroke Response of T-sections (2%, 0.022") .....	48
34. Load-Stroke Response of T-sections (2%, 0.011") .....	49
35. Load-Stroke Response of T-sections (4%, 0.022") .....	50
36. Load-Stroke Response of T-sections (4%, 0.011") .....	51
37. Examples of Fracture in T-Section Tests.....	51
38. Load-Strain Response of T-section Web.....	52
39. Load-Strain Response of T-Section Skins.....	53
40. Delamination Mechanisms in T-sections.....	53
41. Delamination Growth in T-Section with Z-pins .....	54
42. Schematic of DCB/ENF Modeling in DYNA3D .....	56
43. DYNA3D Mesh for DCB Simulation.....	58
44. Unreinforced Specimen Comparison (Load vs. COD).....	60
45. Unreinforced Specimen Comparison (CTL vs. COD).....	61
46. DYNA3D Mesh for Z-pinned DCB Simulation .....	62

## List of Figures

Figure	Page
47. Figure Curve-fitting to Calculate $G_I$ .....	63
48. Load vs. COD Comparison (A-type, $G_{Ic} = 50$ lb/in).....	66
49. CTL vs. COD Comparison (A-type, $G_{Ic} = 50$ lb/in).....	66
50. Load vs. COD Comparison (A-type, $G_{Ic} = 40$ lb/in).....	67
51. CTL vs. COD Comparison (A-type, $G_{Ic} = 40$ lb/in).....	67
52. Load vs. COD Comparison (E-type, $G_{Ic} = 50$ lb/in).....	69
53. CTL vs. COD Comparison (E-type, $G_{Ic} = 50$ lb/in).....	69
54. Load vs. COD Comparison (H-Type, $G_{Ic} = 46$ lb/in).....	70
55. CTL vs. COD Comparison (H-Type, $G_{Ic} = 46$ lb/in).....	70
56. Comparison for Unreinforced ENF Specimen.....	72
57. Comparison of DCB Specimens (Load vs. COD).....	74
58. Comparison of Load vs. CTL in DCB Specimens.....	78
59. COD vs. CTL Comparison of DCB Specimen Tests.....	79
60. Comparison of T-specimen (Load vs. COD).....	80
61. Deformed Shape of T-section Specimens.....	82
62. T-specimen After Testing Showing Z-pins.....	82

## List of Tables

Table	Page
1. Properties of Material Used for DCB Specimens .....	22
2. Z-pinned DCB Specimen Configurations .....	24
3. Z-pinned T-section Specimen Configurations .....	27
4. Elastic Properties of T-Section Web and Skin .....	27
5. Z-pinned DCB Specimen Test Matrix .....	36
6. Test Matrix for T-Specimens .....	46
7. DCB Beam Geometry and Physical Properties .....	59
8. Cohesive Zone Property for the Analytical Model .....	60
9. Cohesive Zone Property in the Z-pin Region .....	65
10. ENF Specimen Geometry and Physical Properties .....	71
11. Cohesive Zone Properties for ENF Model .....	71
12. Peak Load Data in Z-pinned DCB Specimens .....	75

# **MODELING FRACTURE IN Z-PINNED COMPOSITE CO-CURED USING SMEARED PROPERTIES AND COHESIVE ELEMENTS IN DYNA3D**

## **I. Introduction**

### **Scope**

This report describes the results of a combined experimental and analytical study to:

- Investigate mode I, mode II and mixed mode failure response of various composite specimen geometries with through-thickness reinforcement, and
- Verify the DYNA3D smeared property finite element model developed by Adtech Systems Research Inc. (ASRI) by comparing simulation and experimental results.

Specimen geometries tested include: t-section (T-SEC) components as well as double cantilever beam (DCB) and end-notched flexural (ENF) specimens each with and without through-thickness reinforcement. Experiments were conducted “in-house” under low strain rate loading conditions using ASRI and AFRL test facilities.

## **Motivation**

Because of their layered structure, polymer matrix composites (PMC's) do not, in general, have the ability to deform plastically like metals, thus the energy absorption mechanism of composites is different from that of metals. In composites, energy is absorbed by matrix cracking and the creation of large fracture surfaces at the lamina interfaces, a phenomenon known as delamination. Delamination severely impairs the load-carrying capacity and structural integrity of composite structures and since composites naturally lack reinforcement in the thickness direction, delamination is a predominant failure mode. While composites have shown great promise achieving the performance and cost goals of future military aircraft, their use may be limited by their susceptibility to delamination and the need to meet survivability requirements.

The survivability goals for major airframe structural components, defined by the Live Fire Law (1) and the system-specific design specifications have not yet been demonstrated on an all-composite platform. As part of the F-22 program, several ballistic tests were conducted on all-composite wing designs, without success. A survivable design was accomplished only after the wing box was redesigned; replacing three composite spars with five titanium spars. The design changes cost the program thousands of dollars per aircraft, caused a significant schedule slippage and added additional weight to the aircraft. (2, 44-82)

The Air Force and Navy consider the survivability problem of an all-composite structure critical and have invested a significant amount of funding to address this issue. The Air Force's Decoupled Fuel Cells (DFC) program (3) identified the benefits of addressing survivability earlier in the design phase with cost and weight savings using a co-cured wing design for the F-22 and eliminating the titanium spars. The study demonstrated that a wing design that relies on a bolted metal substructure to meet the live fire requirements costs and weighs substantially more than a survivable composite design. Furthermore, the promise of future weight and cost savings can only be realized by addressing the survivability of composite structures early in the aircraft design phase.

The prevailing survivability design procedure is to:

- Develop/identify the survivability requirements for the program
- Size a structure based on design loads (flight, fuel pressure, crash, etc.) and
- Ballistically test the resulting design, using either full-scale articles or large subcomponents, to determine its survivability

For metal structures, this remains a feasible process since there is plenty of historical ballistic test data available for use in developing design requirements.

This is not the case, however, for composite structures.

Advanced processing techniques, interlaminar reinforcement technologies and innovative design concepts have been developed in recent years and provide significant improvements towards achieving survivable, all-composite structures



while minimizing any increase in weight and cost. At the present time several 3D technologies are under investigation toward this end, namely: stitching, tufting, 3D weaving and z-pinning. This paper is concerned solely with the effect of z-pinning.

## **Background**

### Z-pin Processing.

The process for inserting through-the-thickness fibers was developed by Foster-Miller Inc. of Waltham, MA as part of Air Force (4, 94-150) and Naval (5, 93-281) SBIR contracts awarded in 1994 to meet the need for control of delamination. In this technique, short fibers initially contained in dual-density foam are placed in the selected location, on top of an uncured laminate. The foam is used to elastically support the fibers to prevent buckling prior to and during insertion. Z-pins are inserted with the aid of an ultrasonic gun that provides high frequency/low amplitude oscillations causing sufficient energy to be absorbed by the uncured prepreg, allowing the resin to heat up and soften. Direct pressure applied by the insertion gun compacts the foam and causes the orthogonal z-pins to slip easily between the laminate fibers, causing minimal damage. A mechanical vibrating scraper is used to remove the collapsed foam and any excess length of z-pin left on the surface of the laminate. The reinforced laminate is then bagged, cured and processed in the same fashion as would an unreinforced laminate. A

good surface finish as well as a good bond to the inserted z-pins is achieved as the resin flows during the cure process. As a result, z-pinning converts a two-dimensional prepreg lay-up to a three-dimensional composite with little or no change to standard cure cycles.

A range of z-pin preforms exist, characterized by z-pin diameter, the areal density of z-pinning and the initial z-pin length. Figure 1, below, shows z-pins being inserted into a test panel at the Advanced Materials Lab, Air Vehicles Directorate, Wright-Patterson Air Force Base, OH.

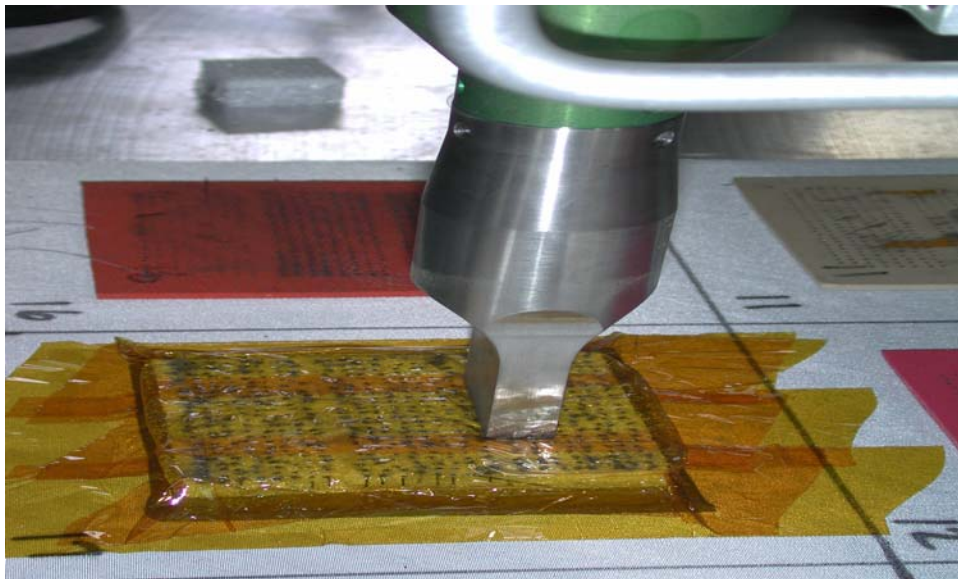


Figure 1. Insertion of Z-pins onto Test Panel  
(Photo courtesy Dr. Stephen Clay, AFRL/VA)

## DYNA3D2000.

DYNA3D (6) is an open source explicit finite element code for analyzing the transient dynamic response of three-dimensional solids and structures. The software is the culmination of various research activities carried out at Lawrence Livermore National Laboratory over a period of more than 20 years. The software package was obtained from Energy Science and Technology Software Center (ESTSC) of the U.S Department of Energy (DOE). The solution procedure in DYNA3D is based on finite element discretization of time.

One-dimensional beams, two-dimensional triangular and quadrilateral shell elements and three-dimensional continuum elements are available for discretizing the finite element mesh. All elements types are capable of handling large deformations and geometric nonlinearity. A total of 52 material models to represent a wide range of material behavior, including elasticity, plasticity, composites, thermal effects and rate dependence are available within DYNA3D. The explicit central difference method is used to integrate the equations of motion in time. The central difference method is conditionally stable, and the stability is governed by the Courant limit on the time step  $\Delta t$ . For solid elements, this limit is essentially the time required for an elastic stress wave to propagate across the shortest dimension of the smallest element in the mesh. Equivalently, this maximum time step may be related to the period of the highest free vibration mode

of the finite element mesh. DYNA3D automatically calculates the maximum time step at each step of the solution, and adjusts the time step accordingly to minimize the number of time steps used in a solution. This feature minimizes the cost of the analysis while assuring that stability is maintained.

DYNA3D uses lumped mass formulation for efficiency. A one point in-plane Gauss quadrature method for numerical integration is available for computational efficiency. The spurious zero energy hourglass deformation modes, which can arise within the elements, are controlled using various stabilization methods available. DYNA3D can also be used to solve quasi-static problems by either using the inbuilt dynamic relaxation option or by simply applying the external loads slowly and integrating the dynamics equations until all significant transient effects die out. A variety of boundary conditions are available including, prescribed velocities, non-reflecting-transmitting boundaries, sliding boundaries and symmetry planes with failure are available. Load can be prescribed either in form of nodal forces and moments, follower forces, surface pressure loads, body force loads, loads due to thermal expansion, loads arising from momentum deposition and airblast loads using Brode functions.

DYNA3D also has a robust and efficient capability for modeling the mechanical interaction of two bodies or two parts of a single body. Fourteen different options, which include frictional sliding, single surface contact, nodes

impacting on a surface tied interfaces, one-dimensional slide lines, rigid walls, material failure along interfaces, penalty and Lagrangian projection options for constraint enforcement and fully automatic contact are offered for defining the behavior of slide surfaces in a wide variety of situations. These options can handle interactions between two surfaces, between discrete nodes and a surface, or between a body and a rigid wall.

DYNA3D can model failure using various techniques and can also handle rigid body dynamics. The input file for a DYNA3D analysis follows a fixed format. The control section is first defined followed by nodes and elements definitions. Next the load curves, loads and initial conditions are defined. The control section for cohesive elements and the cohesive elements connectivity section follow the load definitions. There is no inherent limitation on the size of a DYNA3D analysis model and storage allocation is dynamic within the code. Problem size is constrained only by the memory available on the computer. DYNA3D can be operated on any computer with UNIX or UNICOS operating system.

## **Research Focus**

Preliminary work performed by ASRI studied the response of T-SEC, DCB and ENF specimens reinforced with 0.022” diameter Z-pins. The present research follows the work done by ASRI and differs only in that the T-SEC, DCB and ENF

specimens are reinforced with 0.011” diameter pins. This report, therefore, includes the final results and the background work of the ASRI study insomuch that it is necessary to meet the primary objectives outlined below.

## **Research Objectives**

The goal of this research work is to understand the response of co-cured composite joints with and without z-pin reinforcement, toward this end the objectives are to:

- Test T-section, Double cantilever beam and End-notch flexure specimens reinforced with 0.011” diameter Z-pins
- Add results to existing body of work
- Compare response of 0.022” diameter pin reinforcement to that of 0.011” diameter pins
- Verify existing analytical modeling capabilities with experimental results
- Write and present research results in a thesis

## II. Literature Review

### Overview of Current Research

Z-pin reinforced composites are defined as laminates with up to 5% volume fraction of composite or metallic bridging fibers. A bridging fiber is any fiber extending across a crack connecting both sides of a delaminated laminate.

Because of the large crack opening displacement (COD) that occurs before a z-pin fails, z-pinning is considered a case of large scale bridging (LSB). Under LSB,  $G_{Ic}$  cannot properly characterize the fracture process, which is a small process zone concept. Instead, fiber bridging is described in terms of a bridging law.

Of primary importance in the development of any analytical model designed to simulate the effect of z-pinning is the bridging law or cohesive traction vs. separation relation used to model the behavior and failure of z-pins. The bridging law is the mathematical description of the relationship between the crack opening displacement (COD) and the closure forces imposed by the z-pins. Therefore, the accuracy of the bridging law used in a given model will have a tremendous impact on its ability to correctly simulate the response of a reinforced laminate. However, a trade off exists when developing bridging law equations between those that are most accurate and those that can be solved and modeled without extensive computational expense.

From years of experimental testing, researchers have a good understanding of the bridging law describing the mode I z-pin failure process (7, 8, 9, 10). Research has shown that failure proceeds as follows: 1) as load is initially imposed, the fiber and surrounding matrix, which are initially in a state of negligible stress, begin to stretch elastically. 2) When there is sufficient strain energy, de-bonding of the fiber and matrix occurs along the fiber-matrix interface. 3) Now removed from the surrounding matrix, the reinforcing fiber begins to slide as a rigid body out of the laminate restrained by the frictional forces imposed by the matrix.

In mode II, the two crack faces slide across one another. Cartie et. al. (11) determined that under mode II loading z-pins form as “S” shape, and fail by one of three mechanisms: pin pull-out, internal shear failure or transverse shear failure as shown in Figure 2. The mode II z-pin pullout is a process much like the pullout process described above for mode I with the exception of additional frictional effects caused by the sliding crack faces.



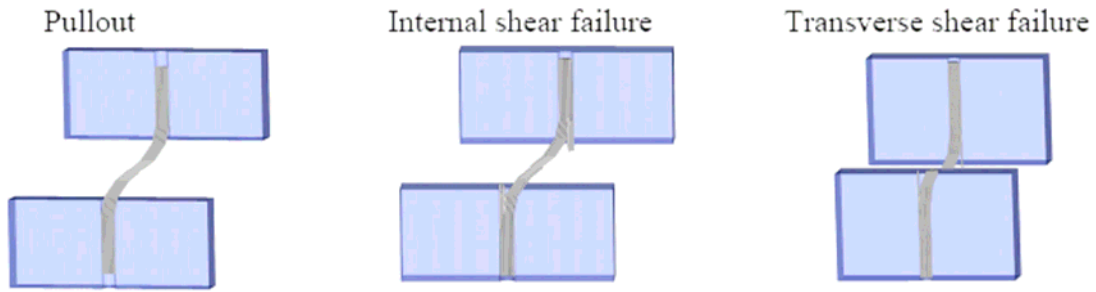


Figure 2. Mode II Z-pin Failure Mechanisms (11, 23)

In certain cases, pins will incompletely pullout of the matrix before it is restrained and ultimately fracture from internal shear stresses. Cartie notes that failure by pin pullout or internal shear involves a small but observable crack opening. Finally, z-pins also fail from transverse shear stresses imposed by the sliding crack faces when there is no pin pullout.

In an un-reinforced composite laminate, very little of the external work done to open the crack is stored as strain energy, most is transformed into surface energy with the creation of new crack surfaces. Strain energy is stored; however, in a reinforced laminate as the extension, delamination and friction forces must be overcome. Zhang et al. (12) analyzed the stress field surrounding a single fiber and determined that only 1-2% of the total energy required to remove a bridging fiber is absorbed during the stretching and de-bonding phases of the test process with the remaining 98% used to overcome the frictional forces imposed by the surrounding matrix as the z-pin is pulled out.

In attempts to simplify an analysis, models have used a variety of bridging functions to simulate the response of reinforced composites. In (13), Liu and Mai included the entire pullout process into the bridging function: elastic deformation, z-pin de-bonding and finally frictional sliding. On the other hand, Jain and Mai (7) used a bridging function that assumed neither an extension nor a de-bonding stage, but rather assumed a constant friction force throughout the test.

The present research attempts to quantify the overall effect of z-pins on the delamination toughness under modes I and II as well as a mixed mode loading condition by treating the z-pinned region as a separate material by smearing fracture properties over the entire area (1 in<sup>2</sup> and 2 in<sup>2</sup>). In order to match the experimental data, the model must, as a basic prerequisite; match the general trend of the bridging law, which as described above involves an increase in load, as energy is stored in the laminate, up to a maximum point after which the load eventually returns to zero.

## **Cohesive Delamination Modeling**

The theory of cohesive modeling of fracture dates back to the work of Dugdale (14) who used the approach to model yielding of steel sheets containing slits. Barrenblatt (15) provided the theory with a solid mathematical foundation. This approach, which models the damage as occurring over a cohesive zone located immediately ahead of the crack tip, provides some structure to predict the

failure process taking place in the vicinity of the crack tip and at the same time addresses the issue of crack tip singularity. One distinguishing feature of this failure process is the assumption that it occurs over a surface rather than being associated with volume of the material. The cohesive zone concept is illustrated in Figure 3 for a Mode I center crack.

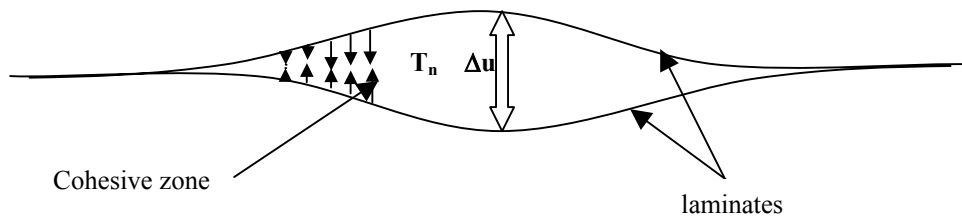


Figure 3. Cohesive Zone Concept

In the cohesive zone, which is the active failure zone, the crack opening is resisted by a distributed tensile cohesive traction ( $T_n$ ) that is a function of the crack opening displacement ( $\Delta U$ ). In the bilinear rate-independent intrinsic cohesive function (16, 17) used in the present research, Figure 4, the traction initially increases with increased transverse displacement, up to the critical value,  $\Delta U_c$ , at which point the stress reaches its maximum value,  $\sigma_{max}$ . Beyond the critical displacement the traction decreases, following a linear law, as the displacement increases to the maximum displacement value,  $\Delta U_{max}$ , beyond which the traction ceases to exist and the crack propagates along the predefined failure path.

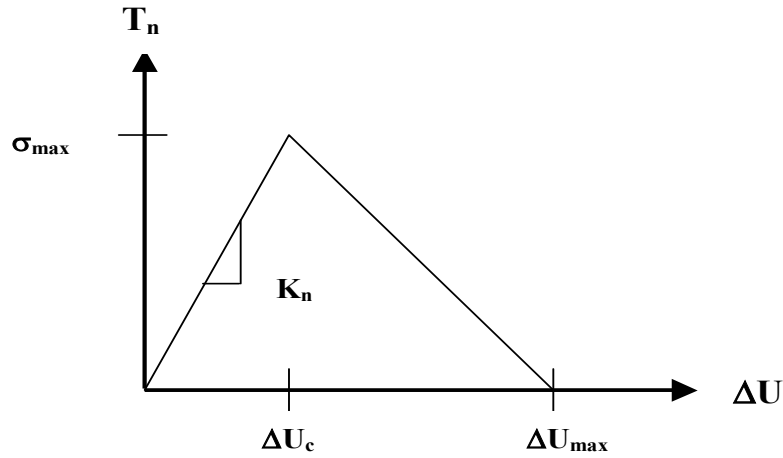


Figure 4. Bilinear Traction Displacement Model

For the case of reinforced DCB specimens loaded in mode I, the rate-independent bilinear cohesive traction-separation law is represented numerically by:

$$T_I = K_I (d) u \quad (2.1)$$

where  $K_I$  is the stiffness matrix and is of the form:

$$K = \begin{bmatrix} K_1 & 0 & 0 \\ 0 & K_2 & 0 \\ 0 & 0 & K_2 \end{bmatrix} \quad (2.2)$$

and  $d$  represents a vector of internal damage variables, which will be described below. For mode II, equation (2.1) holds with  $T_{II}$  and  $K_{II}$  substituted for  $T_I$  and  $K_I$ . DYNA3D is an explicit code and is thus conditionally stable where the internally calculated time step is dependent on the highest eigenvalue in the mesh. If the stiffness matrix is too stiff it can adversely affect the time step calculation for the

problem, thus a judicious choice for  $K_I$  is imperative to ensure stability of the solution.

Toward this end, previous studies (18, 19) have suggested the following empirical relationship for  $K_n$ .

$$K_n = E/h \quad (2.3)$$

Where,  $E$  = Laminate transverse Young's Modulus and  $h$  = sub-laminate thickness. Studies have actually proven that for a given range of values for  $K_n$ , the analysis remains unaffected. Beyond a certain value, however, the solution becomes highly unstable or takes unrealistically long running times, thus it is advisable to use the minimum allowable value for  $K_n$  that reasonably represents the physics of the problem.

The critical stress at which damage initiates under pure mode I loading is given by  $\sigma_1^{cr} = K_1 \times U_1$ . Similarly, the critical stresses at damage initiation under pure mode II is given by  $\sigma_2^{cr} = K_2 \times U_2$ .

The internal damage variable,  $d$ , is calculated according to SNL's original relationship which employs two internal damage variables,  $d_1$  and  $d_2$  to scale the mode I and II stiffness as:

$$K = \begin{bmatrix} K_1 \times d_1 & 0 & 0 \\ 0 & K_2 \times d_2 & 0 \\ 0 & 0 & K_2 \times d_2 \end{bmatrix} \quad (2.4)$$

and generate a bi-linear response under pure mode I or mode II loading. The damage variables initially start at 1 and progress to 0 and are based upon  $U_I$  and  $U_{II}$ , respectively. When  $d_1$  and  $d_2$  are both  $> 1/2$ , the damage variables evolve independently and damage in one mode does not influence the behavior in the other mode. However when both  $d_1$  and  $d_2$ , decrease below  $1/2$ , both are set to the lower of the two values and the damage evolution and response becomes coupled.  $G_I$  and  $G_{II}$  are related to the critical tractions and maximum displacements via:

$$G_1 = \frac{T_1^{cr} x U_1^{\max}}{2} \quad \text{and} \quad G_2 = \frac{T_2^{cr} x U_2^{\max}}{2}, \quad (2.5)$$

respectively. The value for  $G_n$  in equation (2.5) is selected based on the experimental calculation of delamination energy using the area method in our case. The value of  $T^{cr}$  is chosen in a manner to satisfy the constraint of ( $U^{cr} \ll U^{\max}$ ). Very closely spaced values of  $U^{cr}$  and  $U^{\max}$  have shown to introduce dynamic instability in the solution. The value of  $T^{cr}$  has also been shown to not affect the solution for a fairly large range of values (18, 19).

The G value, which was manually calculated, is verified twice, first by comparing it to a curve fit of the results using closed form solutions developed from beam theory and then by comparing results from the DYNA3D model to the original experimental data.

In the un-reinforced region,  $G_{Ic}$  and  $G_{IIc}$  are material properties and may be determined by using any one of a number of available equations. In the z-pinned region, however,  $G_{Ic}$  and  $G_{IIc}$  are, in the most correct sense, not material properties but are a complex function of various attributes such as z-pin material, resin system, z-pin diameter and the aerial density of the z-pins.

## **Cohesive Elements**

The original element formulation and implementation of cohesive elements in DYNA3D was developed by Reedy, et al (19). The cohesive element is a mass-less element with zero thickness sandwiched between two structural elements. The cohesive element should connect two, and only two, shell elements. In addition, the shell elements connected by the delamination elements must reside on opposite faces. Figure 5 illustrates the cohesive element geometry. The instantaneous local mode I direction is established by connecting the adjacent nodes. The mode II and III directions are orthogonal to the mode I direction and point essentially along the mid-surface edges (6).

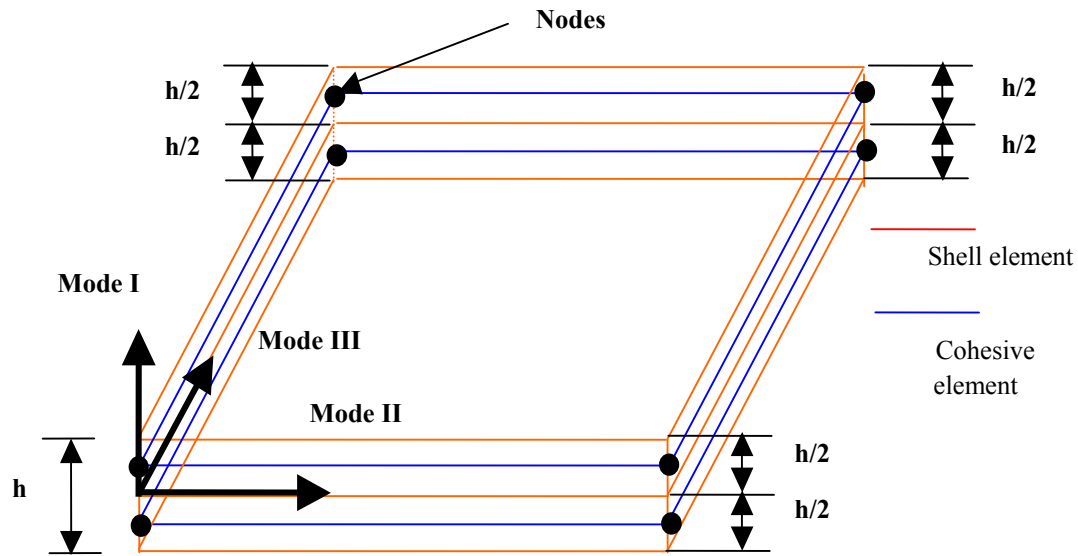


Figure 5. DYNA3D Delamination Element Geometry

The relative mode I displacement across the connection plane is simply equal to the relative nodal displacement in the normal direction (the structural shell elements are inextensible in the transverse direction). Similarly, the mode II displacement across the connection plane is based upon the tangential displacement at the top of the bottom shell. The two shell elements are made to act as a single laminate using a penalty parameter or stiffness matrix,  $K_n$ , as was shown Figure 5.

The cohesive element acts as a nonlinear spring resisting crack propagation along a predefined path in accordance with the traction displacement function. The choice of linearity in the function, as opposed to other cohesive models that use exponential-like functions (20), simplifies the formulation of the cohesive



element and, as will become evident in later sections, is a good choice when used to model z-pins.

Cohesive elements have alternatively been defined as delamination or delam elements within DYNA3D. To be consistent with the DYAN3D definitions, this report refers to interface elements as cohesive elements or delamination elements, both terms referring to the same element.

### **III. Experimental Investigation**

#### **Overview**

The material used to fabricate all test specimens for this investigation is NCT-350-GT145-TR50S graphite fiber/epoxy prepreg obtained from Newport Adhesives and Composites, Inc. Lay-up was performed at AdTech Systems Research Inc. Beavercreek, OH (ASRI). Z-pinning was done by AFRL/VA using pin preforms provided by Aztex Inc., Boston MA (now Albany Engineered Composites, Albany NY). Curing was performed by AFRL/VA and final preparation of specimens was done by AFRL/ML.

#### **Test Specimen Descriptions**

##### Un-reinforced DCB Specimens.

Un-reinforced DCB specimens fabricated for these tests were 9 inches long, 1 inch wide and comprised of twenty-four zero-degree plies stacked to give an overall thickness of 0.12 inches. An initial crack 1” long was incorporated at one end of each specimen at mid thickness using a 0.001” thick Teflon tape separator impregnated into the layers during lay up. Figure 6 illustrates a typical un-reinforced DCB specimen used in this project.

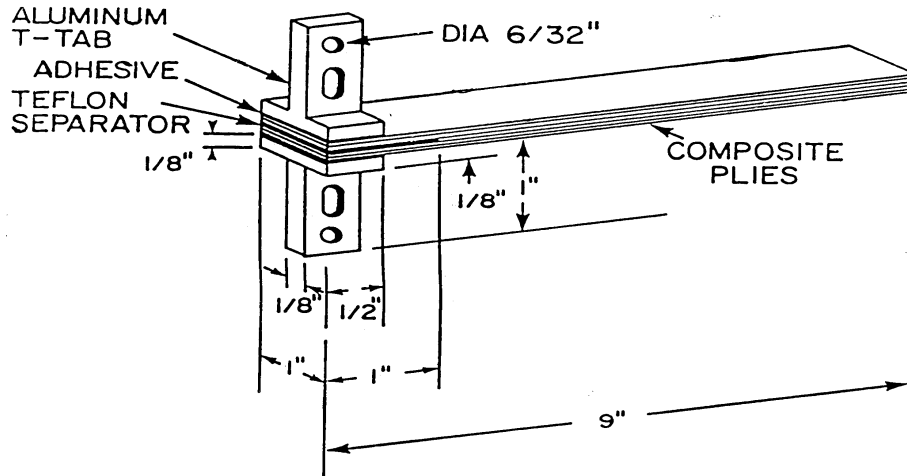


Figure 6. Un-reinforced DCB Specimen Configuration

To determine the elastic properties and strength of the composite material used for the un-reinforced DCB specimens, uni-axial compression and tension tests were performed, by ASRI, on axial and transverse composite coupons. The results of the tests are shown below in Table 1. Each value in Table 1 is the average of four tests.

Table 1. Properties of Material Used for DCB Specimens

	<i>Tension (ksi)</i>		<i>Compression (ksi)</i>	
	E	$\sigma_{ultimate}$	E	$\sigma_{ultimate}$
Axial	17314	144.62	16840	93.63
Transverse	1383	6.40	1215	9.30

### Reinforced (Z-pinned) DCB Specimens.

The geometry of z-pinned DCB specimen is similar to that of an un-reinforced specimen except for the presence of z-pins ahead of the crack. The material (NCT-350-GT145-TR50S) and the tape layout used are the same for both un-reinforced and z-pinned DCB specimens. As seen in Figure 7, a gap of 1" exists between the end of initial crack and the beginning of z-pin region. This region ensures that crack tip blunting does not affect the study of failure processes.

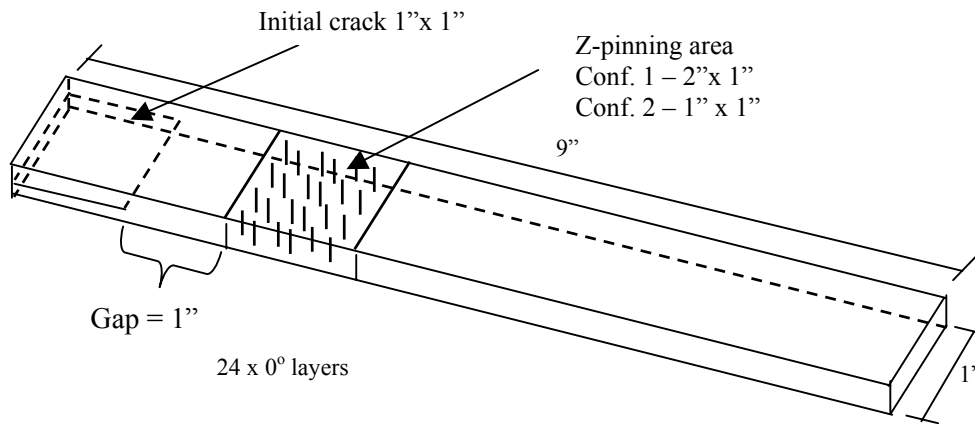


Figure 7. Z-pinned DCB Specimen Configuration

Reinforced DCB testing is divided into eight specimen configurations depending upon: z-pin area/volume density (2%, 4%), z-pin region size (1" x 1", 1" x 2"), and z-pin diameter (0.022", 0.011"), where z-pin area/volume density is defined as the ratio between the total cross-sectional areas, or total volume, of z-pins inserted into a laminate to the total area/volume of the z-pinned region.

Each specimen configuration is designated by letter of the alphabet, as is shown below in Table 2.

Table 2. Z-pinned DCB Specimen Configurations

<b>Configuration Type</b>	<b>Diameter of Z-pin</b>	<b>% of Reinforcement</b>	<b>Area of Z-pinning</b>
A	0.011 inch	2.0	1 inch x 1 inch
B	0.011 inch	4.0	1 inch x 1 inch
C	0.020 inch	2.0	1 inch x 1 inch
D	0.020 inch	4.0	1 inch x 1 inch
E	0.011 inch	2.0	2 inch x 1 inch
F	0.011 inch	4.0	2 inch x 1 inch
G	0.020 inch	2.0	2 inch x 1 inch
H	0.020 inch	4.0	2 inch x 1 inch

Reinforced and Un-reinforced ENF Specimens.

ENF testing is accomplished by applying a three-point bending (TPB) load to reinforced and unreinforced DCB specimens. Therefore, ENF specimens have the same physical, mechanical and geometric properties as the DCB specimens described previously. Z-pinned ENF specimens also share the same z-pin configuration designations as was shown in Table 2. A diagram illustrating the ENF loading condition is shown below in Figure 8.

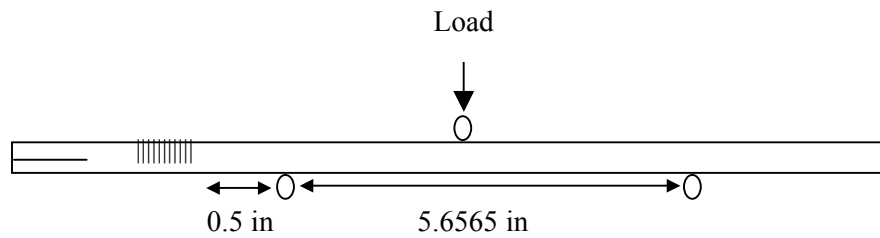


Figure 8. ENF specimen

### Reinforced and Un-reinforced T-Section Specimens.

The T-section test is a mixed mode (modes I & II) fracture test designed to replicate a co-cured, all-composite skin-spar joint within a wing structure. No guidance exists as to the standardization of the test procedure, therefore the test fixture and procedure as well as the specimen size and geometry described below were developed by ASRI.

Aztex Inc. manufactured five configurations of T-section specimens: one with no z-pin reinforcement and four with reinforcement densities of either 2% or 4% for both 0.022” and 0.011” diameter pins. Figure 9 lays out the dimensions of a representative T-section. Different lay-ups make up the skin, web and flanges of the T-sections. Forty layers of a quasi-isotropic lay-up  $[0/90/45/-45]_{5s}$  were used for the skin. For the web, twenty layers of a  $[0/45/90/-45/-45/45/45/90/-45/0]_s$  lay-up, were used. The web divides equally to form the flanges. At the skin-web-flange interface, a resin-rich pocket exists for all T-sections. The three-dimensionally reinforced T-sections are processed with z-pins at the skin-flange interface to demonstrate the effect of through-the-thickness reinforcement

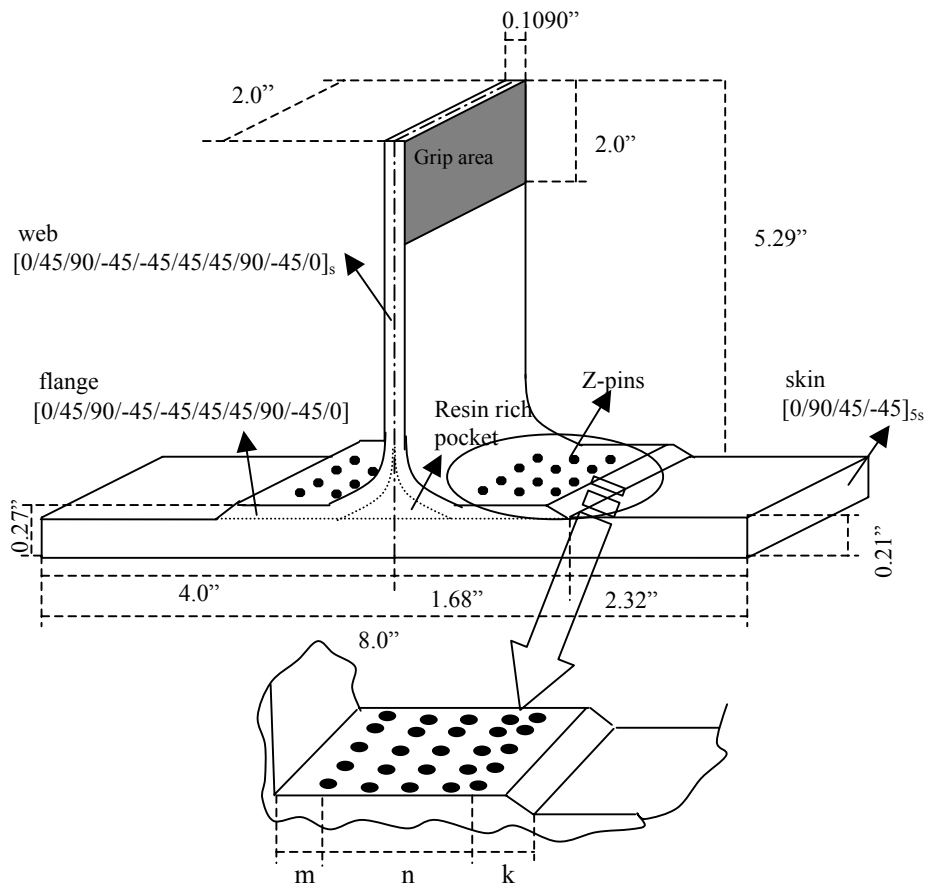


Figure 9. T-Specimen Dimensions and Lay-ups

The dimensions of the z-pinned area differ for 2% and 4% specimens. As shown in the inset of Figure 9,  $m$  represents the distance between the z-pin region's inner edge and the web, the length of the z-pin region is represented by  $n$ , and the length between the outer edge of the z-pin region and the end of tapered section is expressed as  $k$ . The corresponding values of  $m$ ,  $n$ , and  $k$  for both specimen densities are listed in Table 3.

Table 3. Z-pinned T-section Specimen Configurations

Z-pin %	m (in.)	n (in.)	k (in.)
2%	0.2955	0.8745	0.4555
4%	0.2955	1.329	0.001

Coupon-type specimens were prepared using lay-ups matching those of both the T-section web and skin. Uniaxial tension and four-point bending tests were performed by ASRI to determine the elastic modulus and Poisson’s ratio for each lay-up. Table 4 summarizes the experimental results.

Table 4. Elastic Properties of T-Section Web and Skin

	<i>Web</i>		<i>Skin (ksi)</i>	
	E (ksi)	$\nu$	E (ksi)	$\nu$
Axial	6400	0.45	8290	0.38
Flexural	6408	--	8310	--

Material variability and stress concentration regions in T-sections with and without z-pins were observed as ASRI performed a thermoelastic stress analysis (TSA) using a DeltaTherm DT1500 measurement system with infrared camera. Cyclic loads were applied using an MTS 810 servo-hydraulic test system. The DeltaTherm infrared array detector synchronized with the applied cyclical loading enables detection of the transient thermoelastic effect. Application of direct mechanical cyclic loads creates a temperature change in the material with the



amount of temperature change being different in different areas. Figure 10 shows a schematic of the TSA test setup.

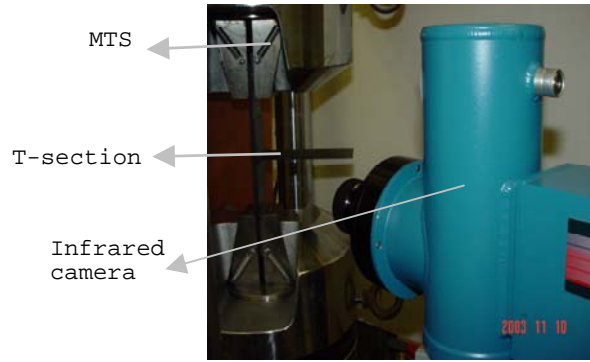


Figure 10. TSA Test Set-up

Figure 11 presents the temperature fields of T-sections with and without z-pins, taken by infrared camera at a 1000 lb load level, 750 lb load amplitude and frequency of 5 Hz. Yellow areas in the figure indicate regions of highest stress concentration under the applied loads. Two areas of high stress concentration exist for T-sections with and without z-pin reinforcement, the resin rich area at the skin-web-flange interface and the tapered-end of the skin-flange interface. Therefore, initial failure is to be expected at one of these locations.

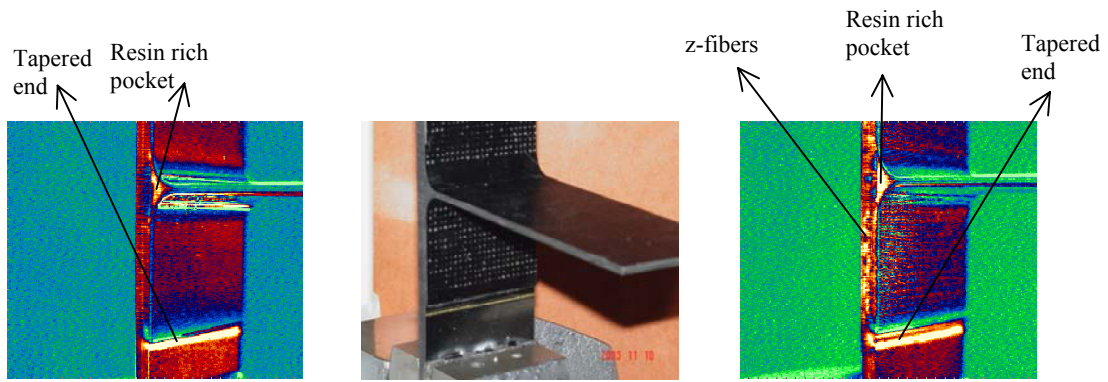


Figure 11. TSA Infrared Camera Pictures

Existence of additional stress concentration regions in T-sections with z-pins can be attributed to: the addition of different material (z-pin) to the original lay-up, separation of in-plane fibers during pinning, and the existence of residual stresses at z-pin locations. Steeves and Fleck (20) analyzed the effect z-pinning has on laminate in-plane properties. Their work showed that z-pins cause a misalignment of laminate fibers and resin rich pockets, resulting in stress concentrations and tensile and compressive composite strength reductions of 27% and 30%, respectively.

## Testing

### Double Cantilever Beam (DCB) Tests.

Experimental testing of DCB specimens was carried out on MTS machines at ASRI's testing laboratory. 0.5" and 1" tabs were used for un-reinforced and z-pinned DCB specimens, respectively. A wire-break measurement technique, developed by ASRI and based on electric potential drop principles, was

implemented to track crack growth. The circuit setup and wiring attaching the DCB specimen to the MTS machine are shown in Figure 12. The method produced good crack propagation measurements that were electronically recorded as tests progressed. Analysis of experiments with and without crack growth tracking wires showed the wires have a negligible effect on the experimental response of the specimens.

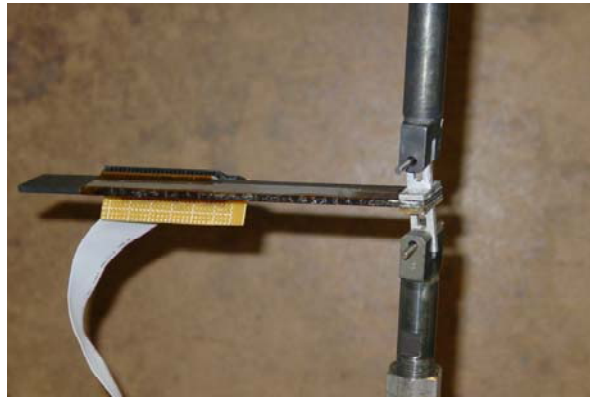


Figure 12. DCB Specimen with Crack Measurement Gage

Figure 13 is a picture of the crack tip-locator gage used. The printed circuit board strip automatically tracks crack propagation in increments of 0.25” eliminating the need for visual tracking of cracks using marker fluid.

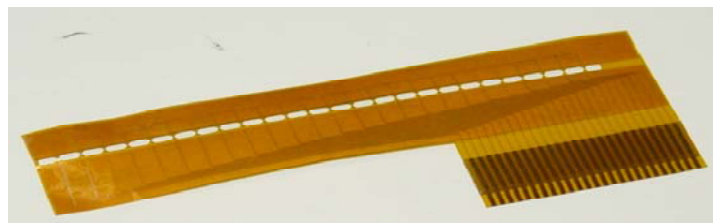


Figure 13. Crack Locator Gage

### Un-reinforced DCB Tests.

Testing of un-reinforced DCB specimens was performed by ASRI on an MTS machine at quasi-steady crosshead rates of 0.1, 1.0, 30.0, and 60.0 in./min. Figure 14 shows load vs. crack opening displacement (COD) curves for each test. Similar responses were obtained for each test rate.

Curves for crack locator voltage (CLV) vs. COD are shown in Figure 15. Crack locator voltage indicates the crack tip location (CTL) within the specimen. As seen in Figures 14 and 15, crack growth in all DCB specimens is similar. Therefore, there is no effect due to the application of different displacement rates within this range (0.1-60.0 in/min).

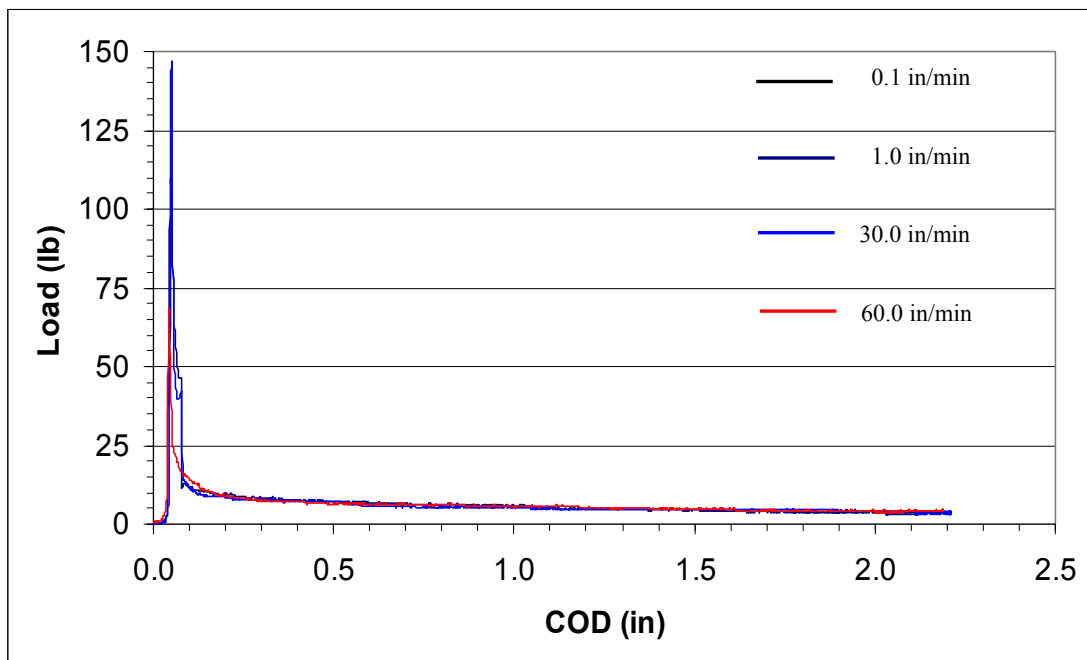


Figure 14. Load vs. COD for Un-reinforced DCB Specimens

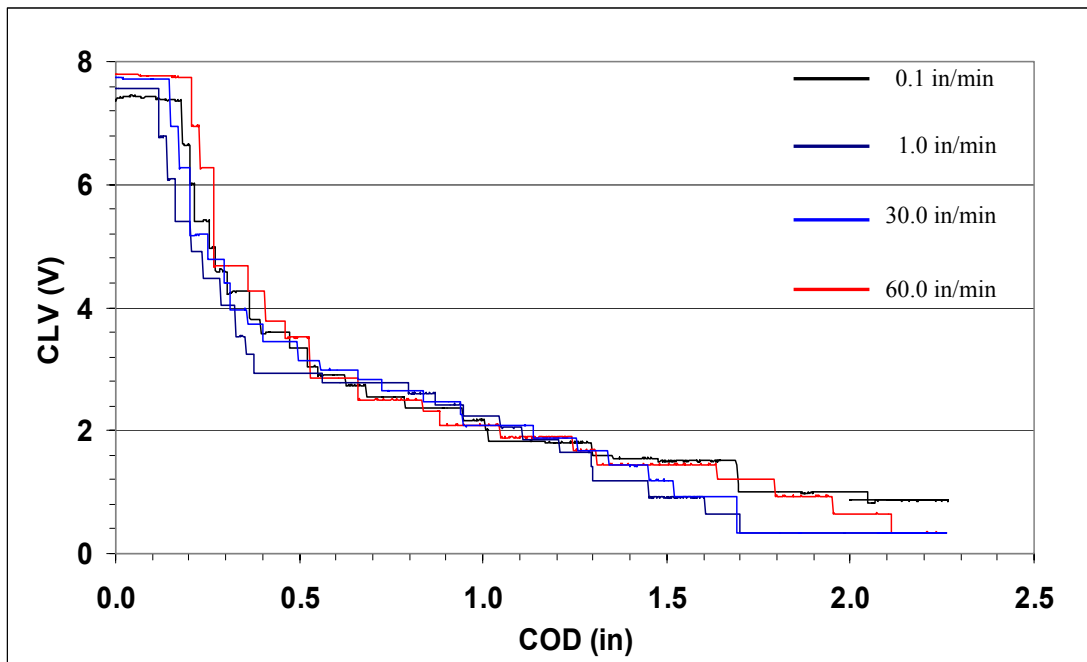


Figure 15. CLV vs. COD for Un-reinforced DCB Specimens

#### Reinforced (Z-pinned) DCB Tests.

In the first part of z-pinned DCB testing an experimental study to observe the effect of different loading rates on z-pinned DCB specimens was first performed by ASRI. For this reason, three tests using A-type z-pinned DCB specimens were carried out at displacement rates of 0.1, 30, and 74 in/min. Figure 16 shows load vs. COD responses obtained from each test.

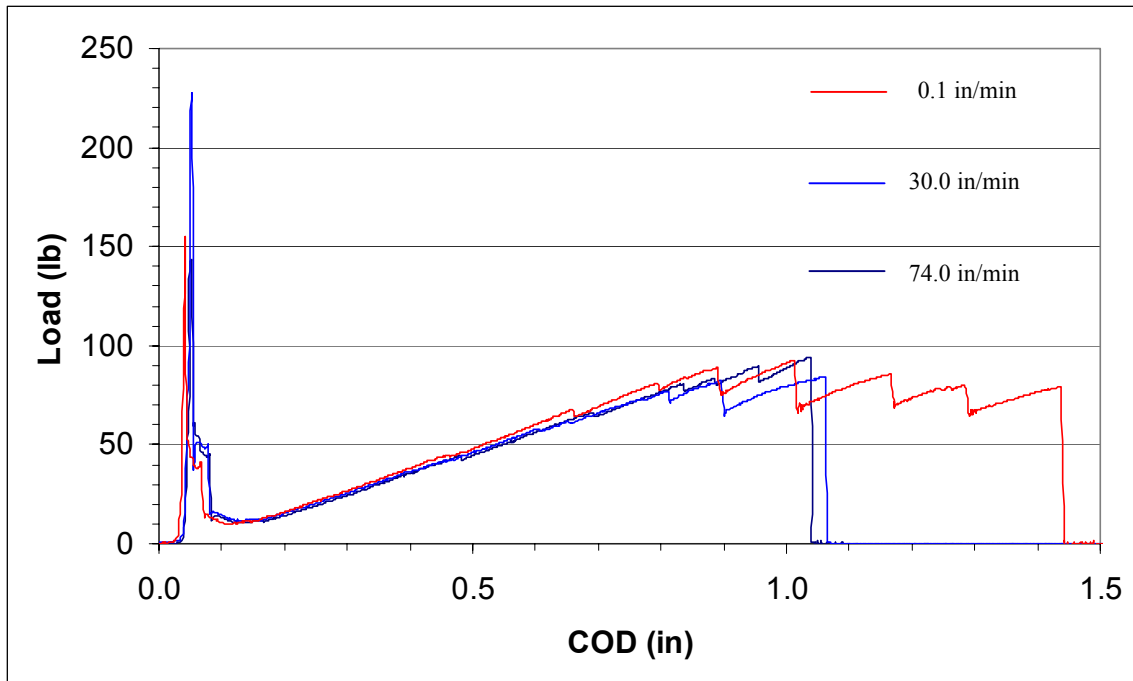


Figure 16. Load vs. COD for A-type Z-pinned DCB Specimens

As seen in the figure, the response at different displacement rates is essentially the same. At 0.1 in/min, the specimen failed immediately after the crack reached the end of the z-pin area. However, at 30 in/min and 74 in/min, the tabs de-bonded while the crack was propagating through the z-pin region. Despite the unexpected failure, Figure 16 indicates that the application of different displacement rates has no effect on specimen's response as was the case for the un-reinforced DCB specimens. Comparing Figures 14 and 16 reveals that regardless of displacement rate, the interlaminar toughness of the material experiences an enormous increase through the z-pin region.

Observations from z-pinned DCB experiments are expressed quantitatively in terms of two representative plots: crack-tip location (CTL) vs. COD and load vs. COD as shown in Figures 17 and 18.

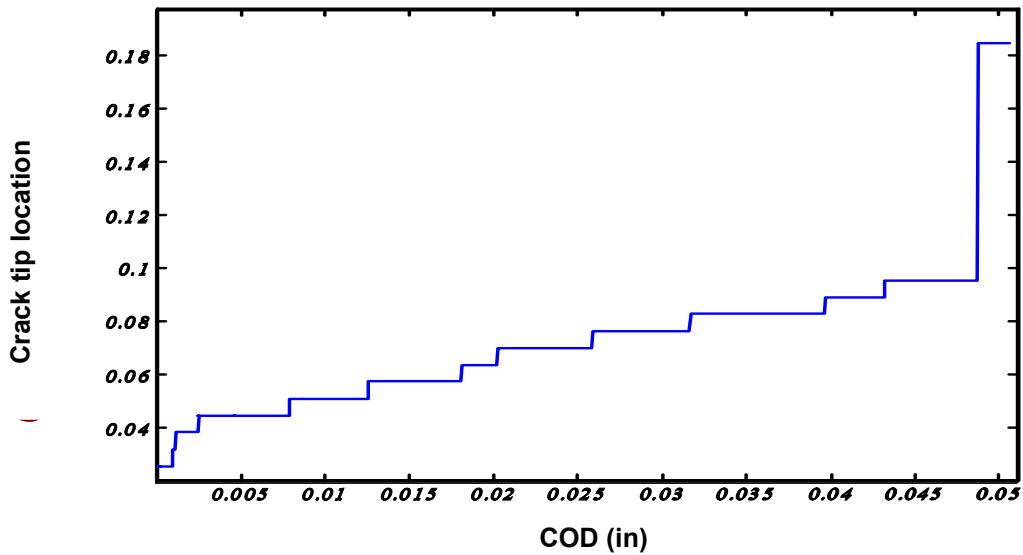


Figure 17. CTL vs. COD for a Representative Z-pinned DCB Specimen

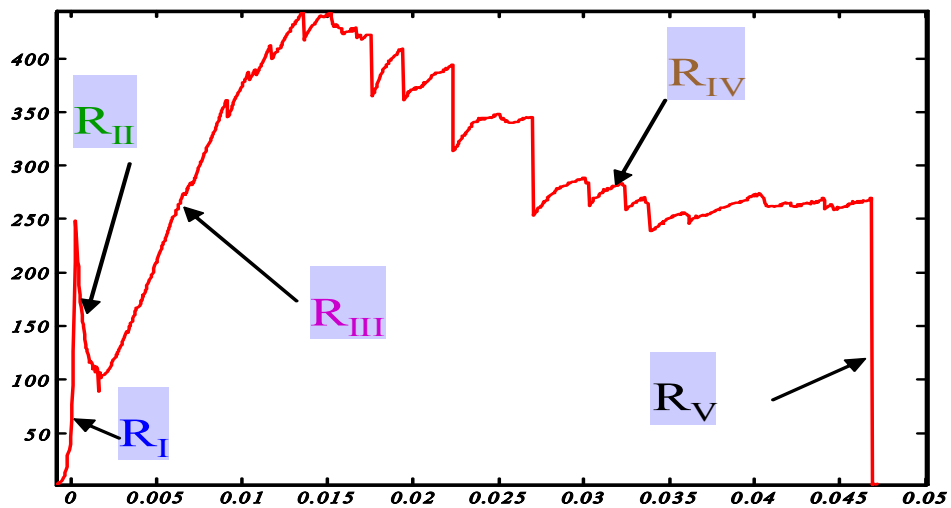


Figure 18. Load vs. COD for a Representative Z-pinned DCB Specimen

As shown in Figure 18, there are five important regions in the Mode I fracture process of the z-pinned DCB specimen:

- R<sub>I</sub> – Region of no crack propagation and quickly increasing load; ends as initial blunt crack is overcome
- R<sub>II</sub> – Steady state crack growth in un-reinforced region between blunt crack and first z-pin row; ends as sharp crack encounters first z-pin row
- R<sub>III</sub> – Linear region of increasing load and slow crack growth due to z-pin reinforcement; ends after first z-pin row failure
- R<sub>IV</sub> – Steady state crack propagation region through z-pin Reinforcement; ends after final z-pin row fails
- R<sub>V</sub> – Rapid crack growth out of z-pin reinforced region

Figure 19 illustrates how Figures 17 and 18 work together presenting COD vs. both load and crack tip location for a representative z-pinned DCB specimen.

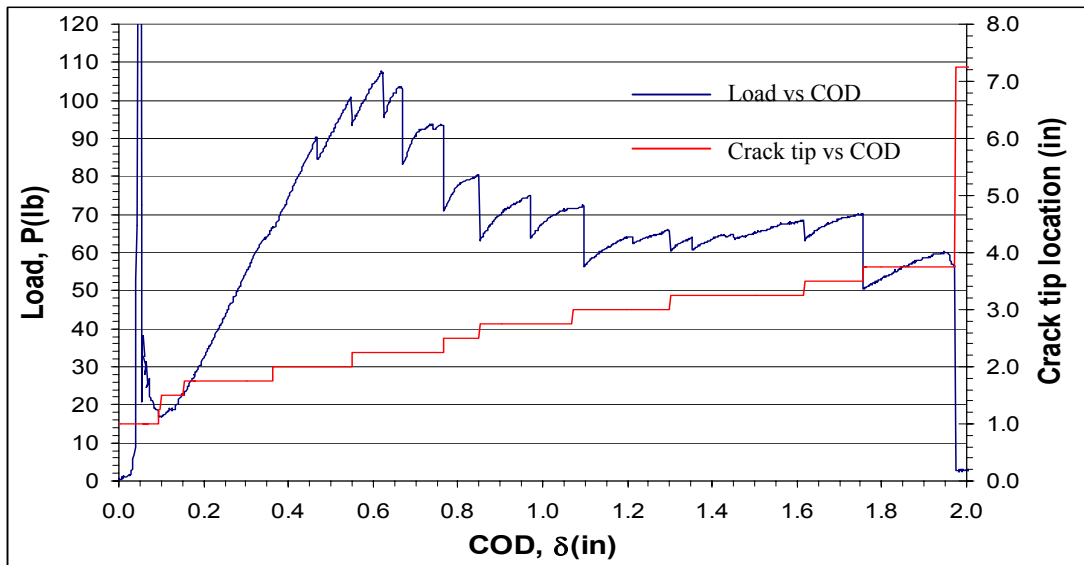


Figure 19. COD vs. Load/CTL (Representative DCB Specimen)



In the figure, each load drop-off on the blue curve, such as at 90 lb (COD = 0.45”), corresponds to a jump in crack tip location on the red curve. In this case, the jump is from 2.0” to 2.25”, the location of the first z-pin row. When total failure of the specimen occurs at a COD of 1.97”, the crack tip jumps suddenly from 4” to 7”.

In the second part of z-pinned DCB specimen testing, a total of sixteen tests were carried out using A, B, E, F, G and H-type specimens, as tabulated in Table 5, each utilizing a displacement rate of 0.1 in/min. The purpose of these tests is to compare the response of z-pinned DCB specimens with different z-pin densities, diameters and reinforcement areas. Figures 19 through 24 display the load vs. COD curves for each z-pin configuration listed in Table 5.

Table 5. Z-pinned DCB Specimen Test Matrix

Number of tests	Specimen type	% of z-pin	Diameter of Pin	Z-Pin Area
2	A	2%	0.011"	1" X 1"
2	B	4%	0.011"	1" X 1"
2	E	2%	0.011"	2" X 1"
2	F	4%	0.011"	2" X 1"
4	G	2%	0.022"	2" X 1"
4	H	4%	0.022"	2" X 1"

Figures 20 and 21 illustrate the response of specimens reinforced with 0.022” diameter pins (G and H-type specimens), while Figures 22 – 25 depicts the response for specimens with 0.011” diameter pins (A, B, E and F-types). Of the six z-pinned DCB specimen configurations tested, the E, F, G and H-type specimens have the same reinforcement region (1” x 2”) and will be used predominantly in the comparisons that follow.

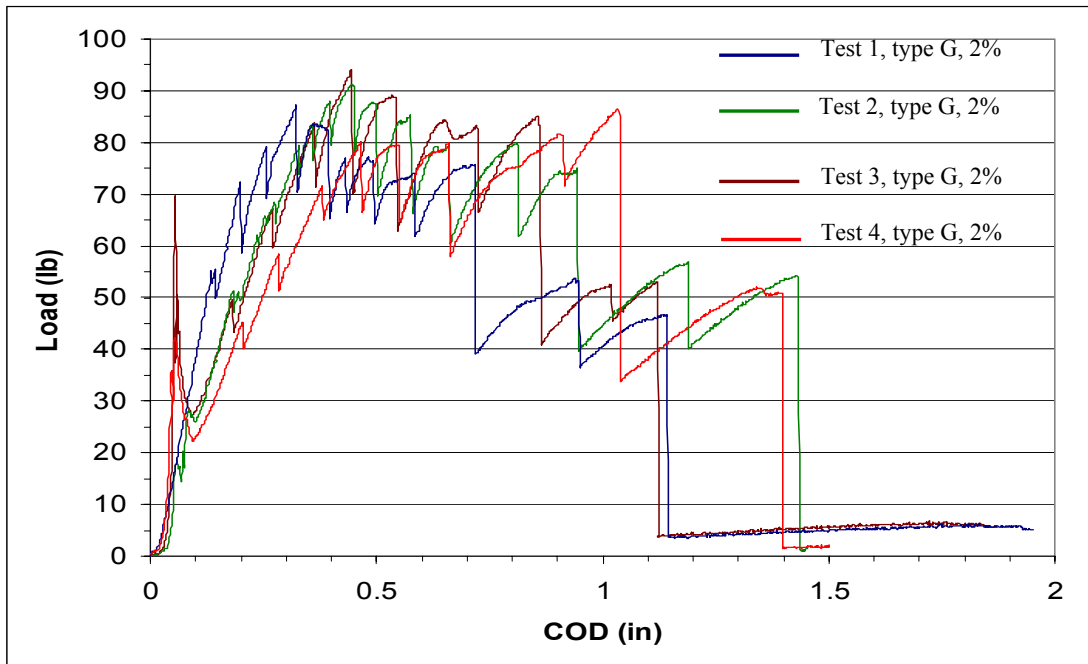


Figure 20. Load vs. COD, G-Type Z-pinned DCB Specimens

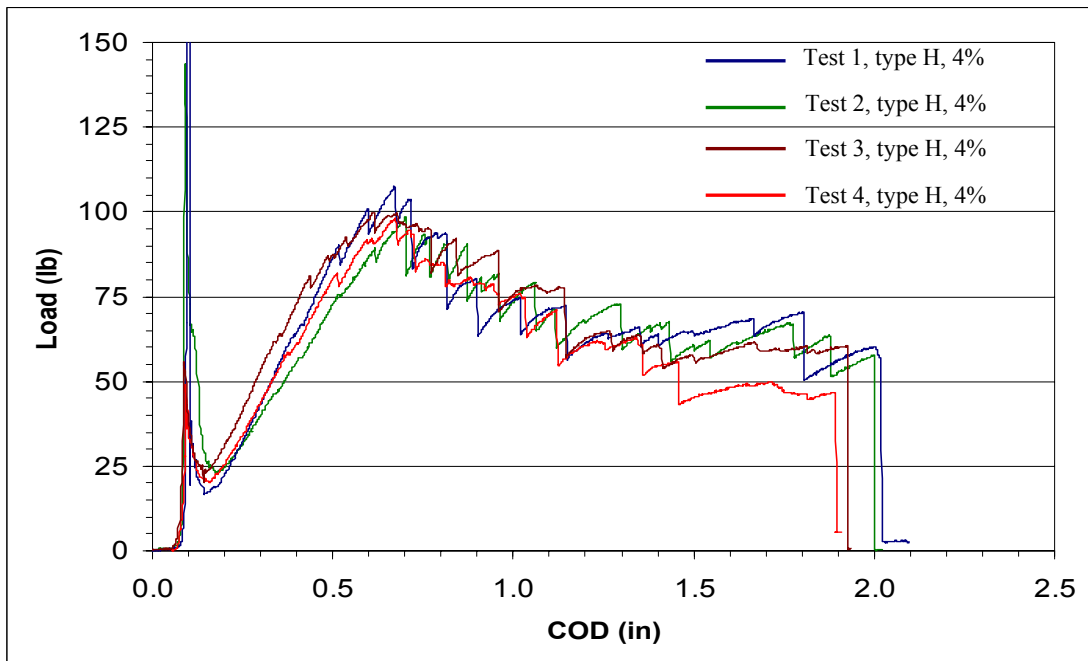


Figure 21. Load vs. COD, H-Type Z-pinned DCB Specimens

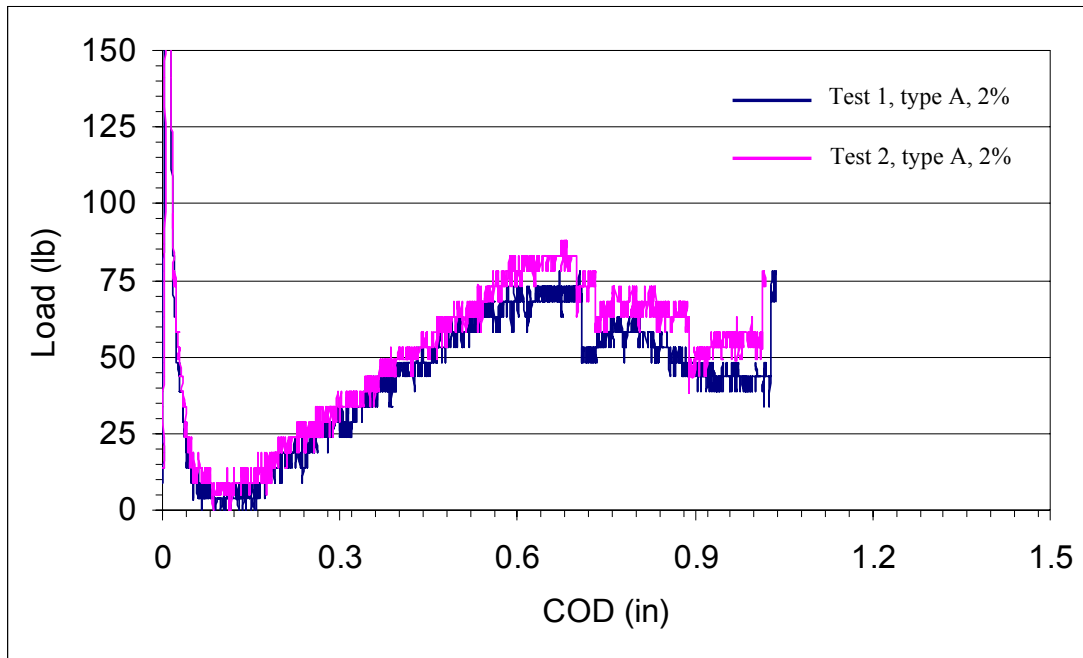


Figure 22. Load vs. COD, A-Type Z-pinned DCB Specimens

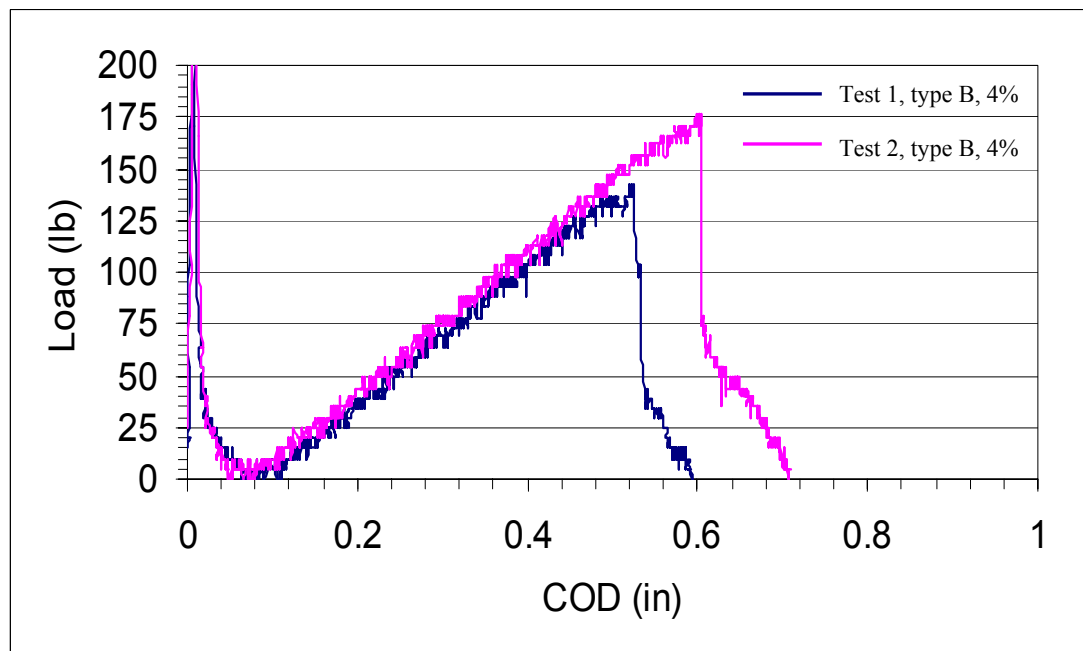


Figure 23. Load vs. COD, B-Type Z-pinned DCB Specimens

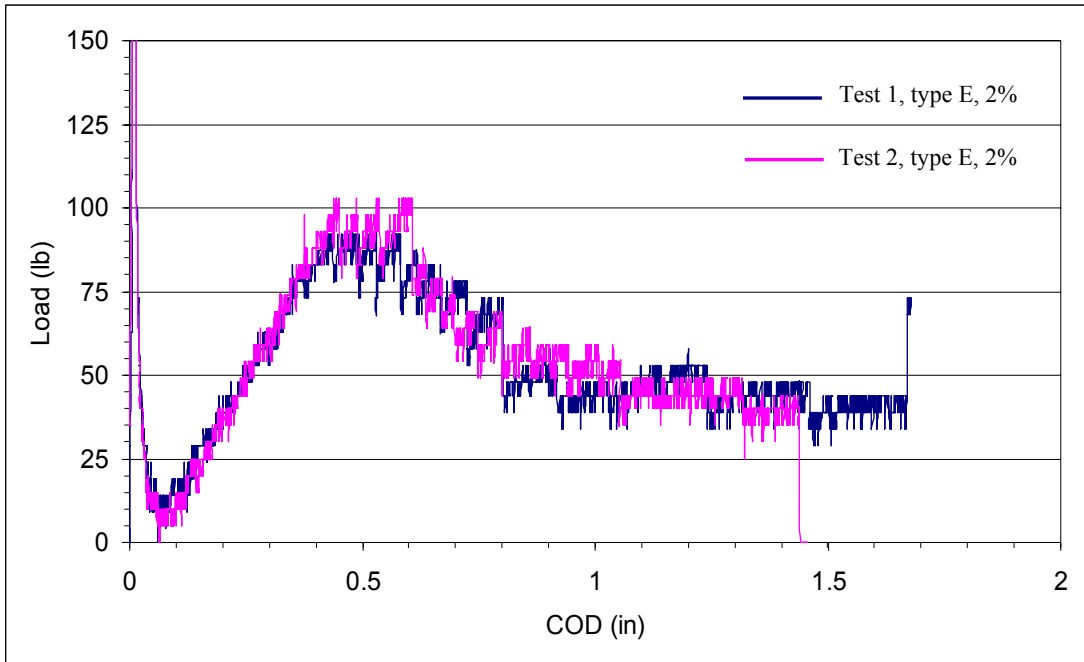


Figure 24. Load vs. COD, E-Type Z-pinned DCB Specimens

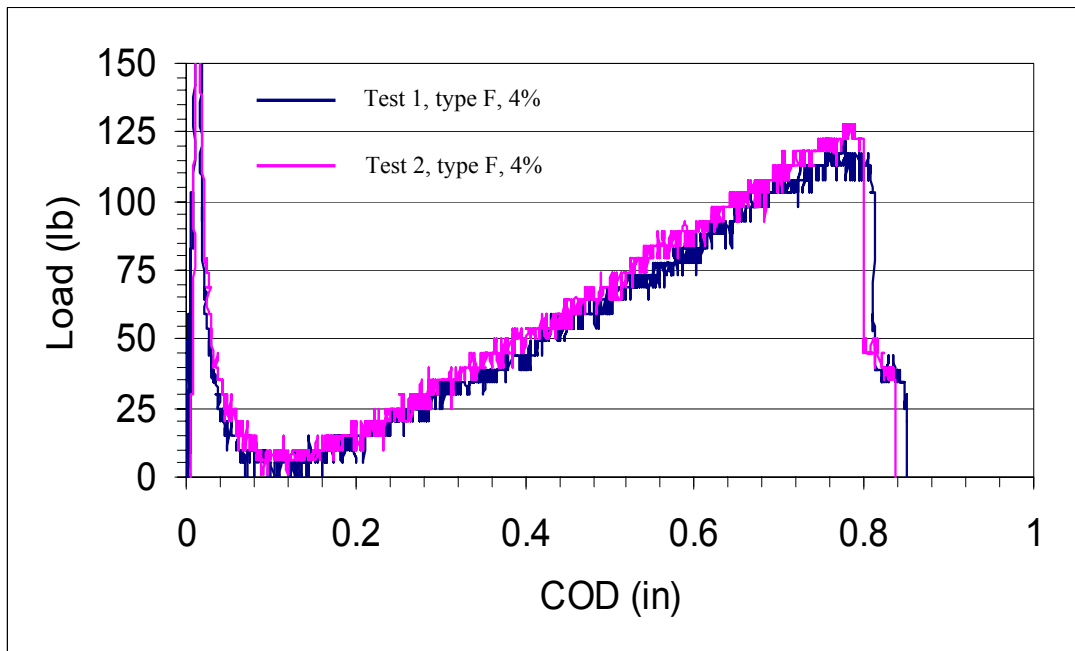


Figure 25. Load vs. COD, F-Type Z-pinned DCB Specimens

The reader will note in comparing Figures 21, 23 and 25 the abrupt failure of the B and F-type specimens. Each of the three specimen types has 4% reinforcement density and a similar response as load is increased up to the peak load. Beyond peak load the specimen reinforced with 0.022" diameter pins failed in an expected manner as the crack progressed through the z-pinned region while the specimen reinforced with 0.011" diameter pins failed suddenly as the half-laminate fractured due to excessive bending load. This unexpected failure mode, shown in Figure 26, occurred in each of the four tests of specimens reinforced with 0.011" pins at 4% density (both 1 in<sup>2</sup> and 2 in<sup>2</sup> areas).

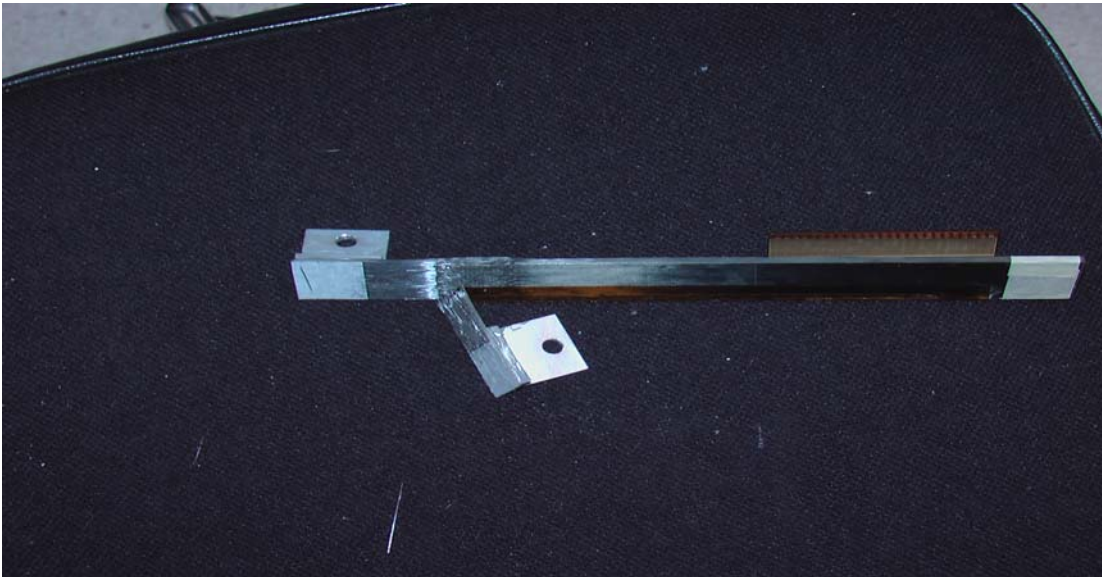


Figure 26. Unexpected Fracture of DCB Specimen

### Un-reinforced and Reinforced ENF Tests

Experimental testing of ENF specimens was performed at the ASRI laboratory on MTS machines at a constant displacement rate of 0.1 in/min. At present, no effort has been made to determine the effect different displacement rates have on ENF load-COD behavior.

Because of pressure applied to the specimen's width, the wire-break measurement tool used to track crack growth in DCB tests could not be used during ENF testing. Instead, the specimen thickness was painted with white marker fluid and crack growth was monitored visually. Figures 27 and 28 show the load vs. mid-span deflection response of un-reinforced and reinforced ENF specimens, respectively. There is no appreciable difference in the figures.

In un-reinforced ENF testing, crack propagation occurred as expected, but in reinforced tests, the blunt crack progress was never overcome and the entire specimen fractured, as seen in Figure 29. Attempts were made to open the blunt crack in order to assist crack growth, without success. What is interesting in comparing the un-reinforced and reinforced test data is that although failure occurred in two very different manners, the load and COD at failure for both test types are essentially the same.

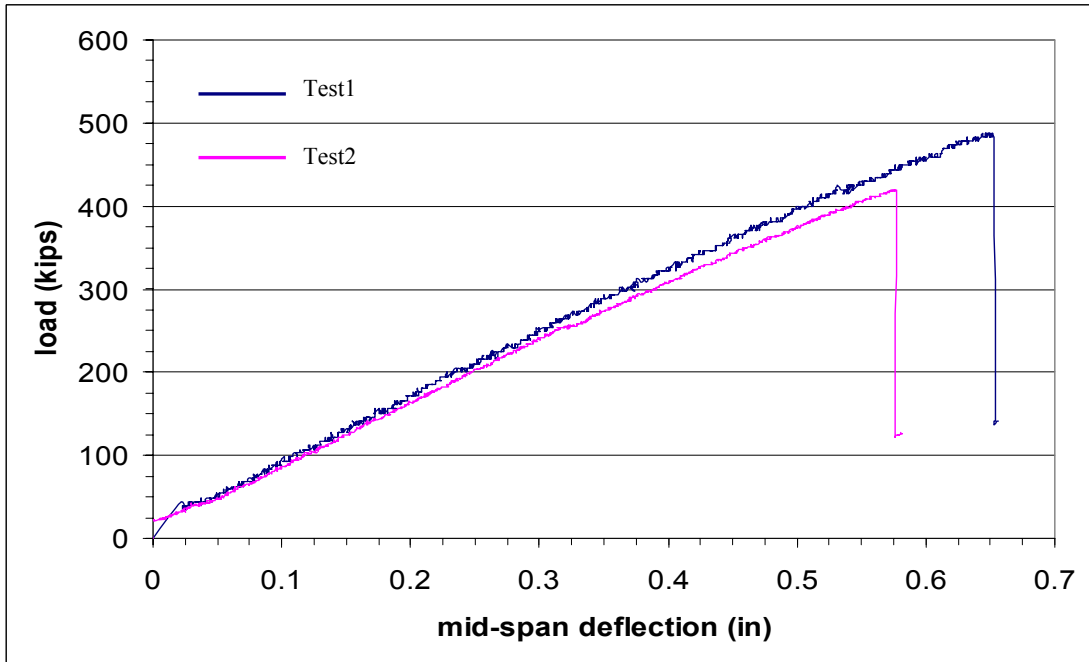


Figure 27. Un-reinforced ENF Test Results

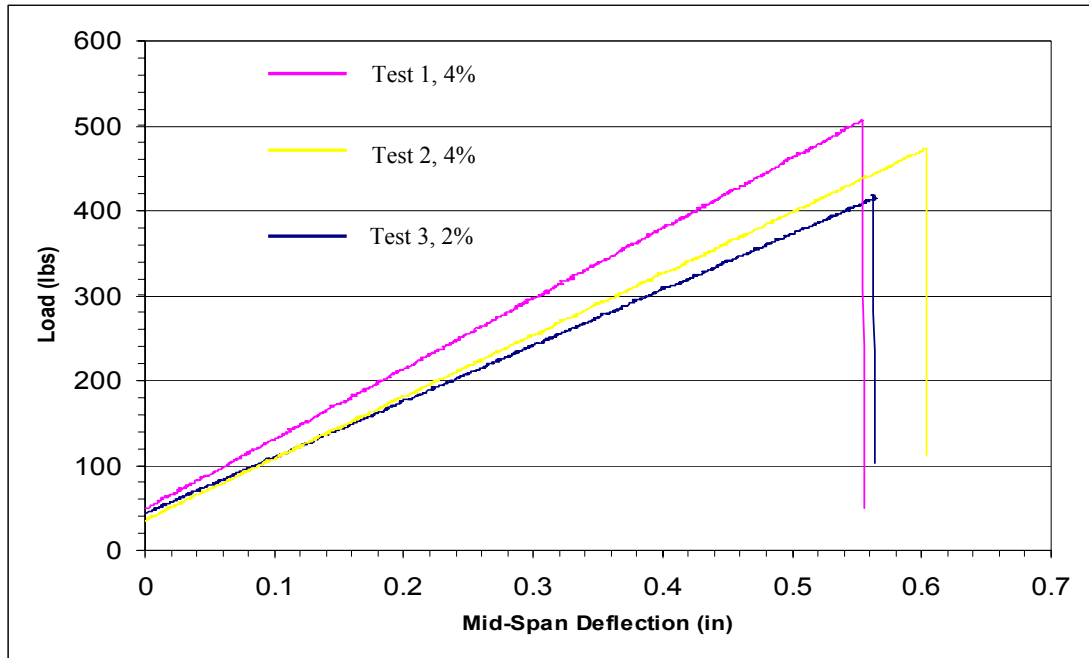


Figure 28. Reinforced (Z-pinned) ENF test results



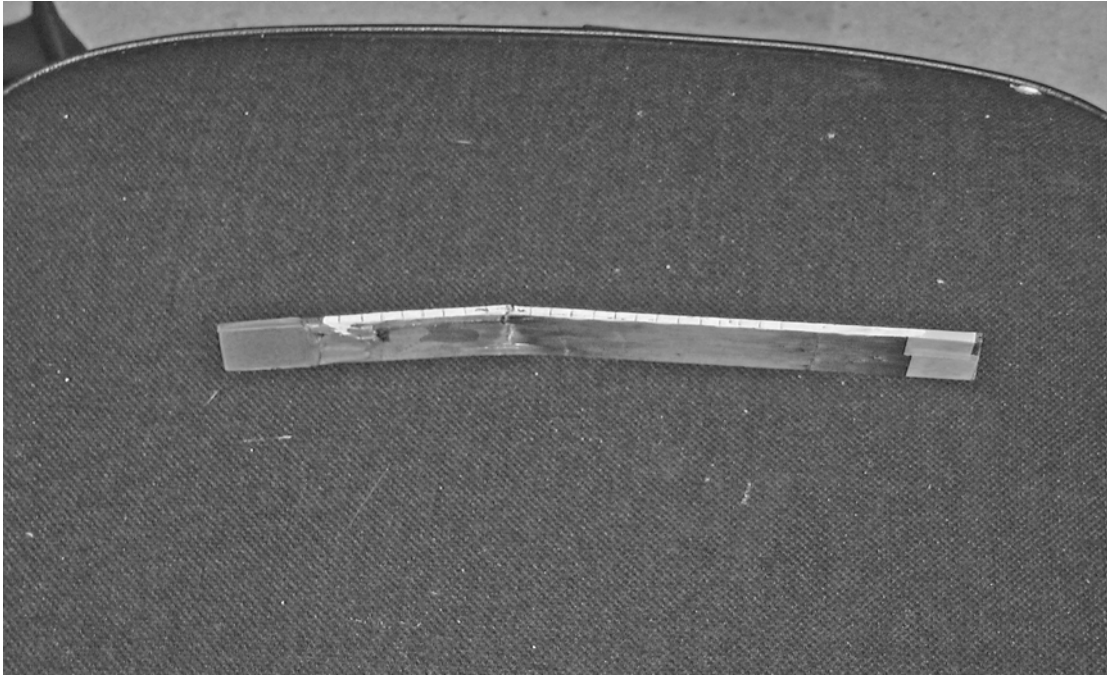


Figure 29. Unexpected Fracture of Z-pinned ENF Specimen

There are examples of researchers using the ENF geometry in computer simulations to model the mode II response of z-pinned composites (21, 22); however the primary body of experimental research utilizes geometries other than the three-point bend ENF test (23). Cartie et. al (11) produced good results using a “mini three-point-bend ENF” test specimen at reinforcement densities up to 2%, but this is the only work found to have performed physical tests using a similar test set up. In (11) mention is made of problems involving catastrophic failure of ENF tests, but no description of the type of failure is given.

Regardless, future reinforced mode II testing accomplished for this project is planned to utilize a four-point bend test set-up to reduce the bending moment and the possibility of this type of fracture.

#### Unreinforced and Reinforced T-Section Tests.

All T-section specimens were tested at room temperature using a 20-kip MTS machine and a three-point bend (TPB) test fixture as seen in Figure 30. In total, twelve specimens with differing pin sizes and densities were tested under TPB loading according to Table 6, shown below. All tests were run at a displacement rate of 0.02 in/min.

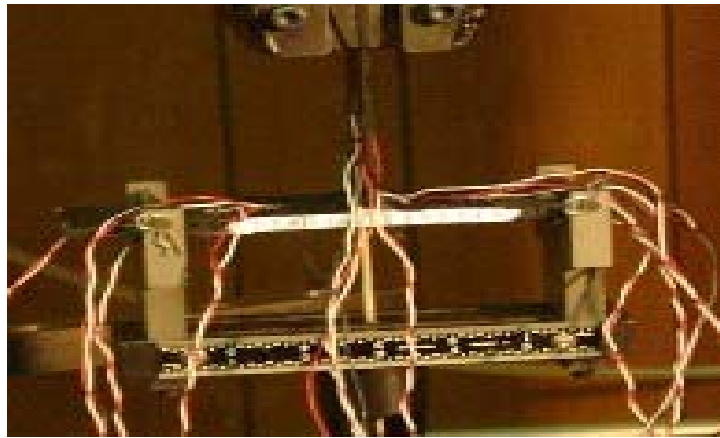


Figure 30. TPB test fixture

Table 6. Test Matrix for T-Specimens

Number of tests	Specimen type	z-pin Density	Diameter of Pin
3	W	2%	0.011"
3	X	4%	0.011"
2	Y	2%	0.020"
2	Z	4%	0.020"
2	Unreinforced	0%	N/A

Figure 31 is a schematic diagram of the support and strain gage locations for a representative T-specimen. Figure 32 is a photograph of the Vishay CEA-06-125UN-350 strain gage used in T-specimen testing.

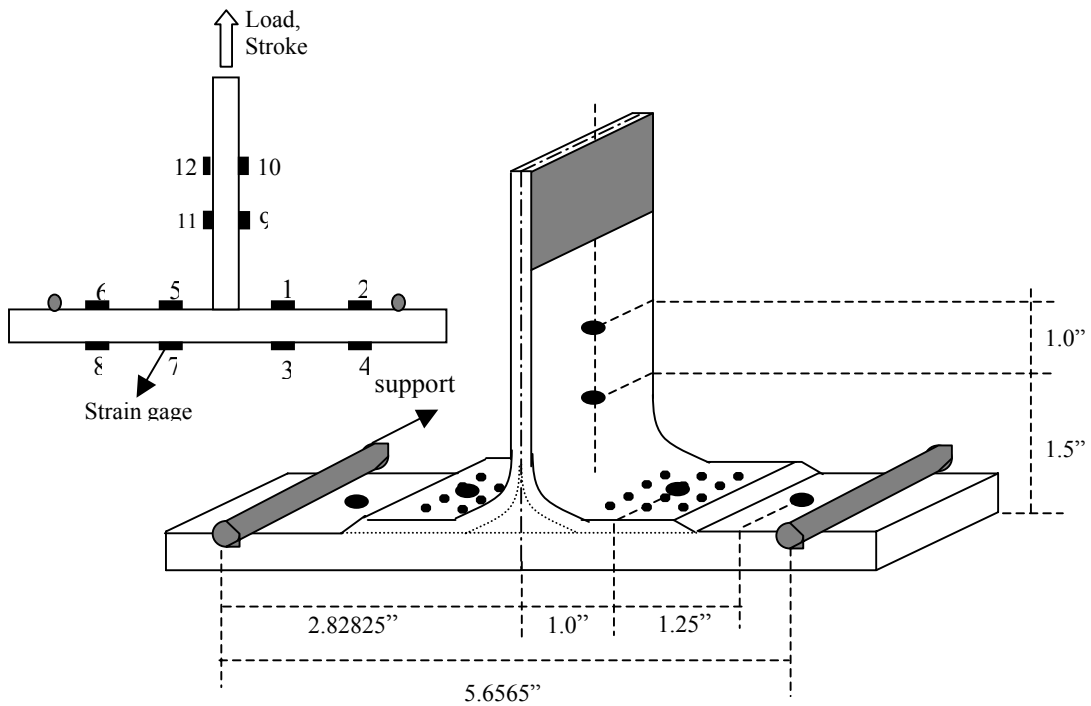


Figure 31. T-Specimen Strain Gage and Support Locations

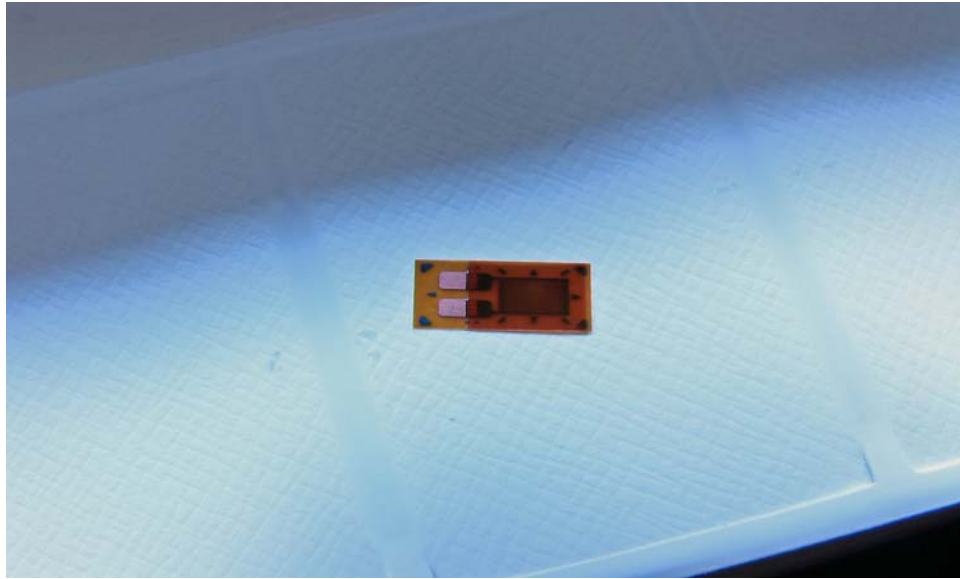


Figure 32. Vishay CEA-06-125UN-350 Strain Gage

The load-stroke response of each configuration of T-specimen listed in Table 6 is displayed in Figures 33 – 36. In Figure 33 (0.022”) Test 2 clearly has a lower initial failure load than Test 1 and could not reach the maximum load experienced in Test 1. The initial slopes and failure displacements of both specimens however, are the same. Additionally, fewer load-drop points exist due to z-pin row failure in Test 1 than Test 2. This is due to multiple z-pin rows failing simultaneously in Test 2; for example, at a stroke value of 0.3 in.

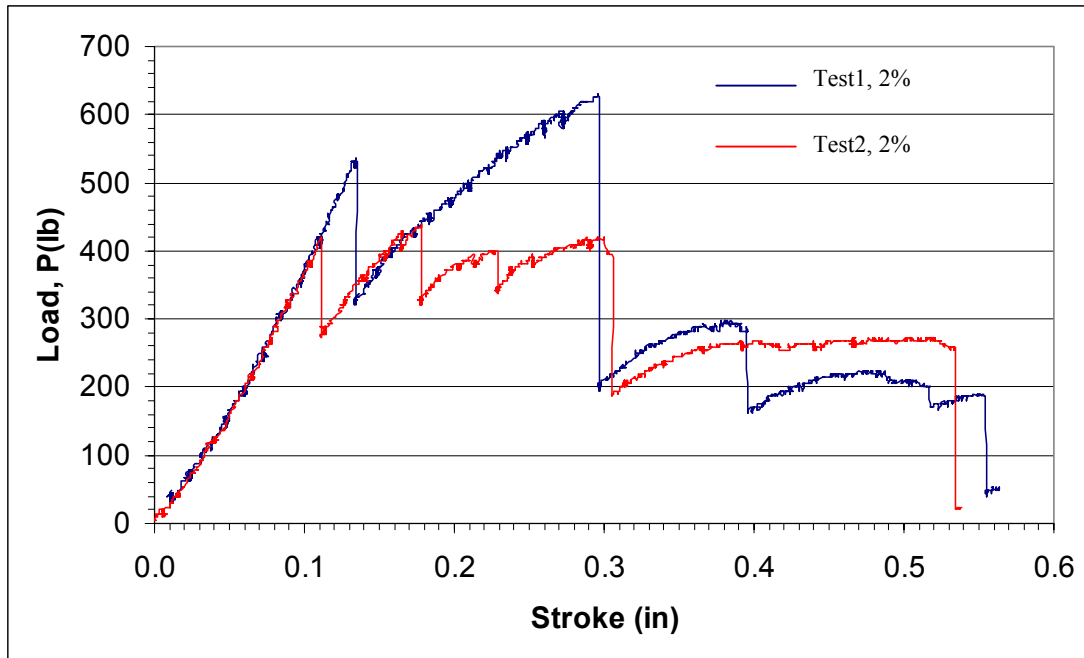


Figure 33. Load-Stroke Response of T-sections (2%, 0.022'')

Figure 34 illustrates that T-specimens reinforced with 0.011'' fail suddenly, as the delamination traverses the entire z-pinned region when failure load is reached. Comparing Figures 33 and 34 shows that final failure displacement for both specimen configurations occurs at 0.55 in, while specimens reinforced with 0.011'' pins reached a 25% higher peak load that did the specimens using the 0.022'' pins. A comparison of the area beneath the curves in Figures 33 and 34 reveals that the failure energy for specimens with 0.011'' pins is three times greater than that of specimens with 0.022'' pins when both have a 2% areal pin density.

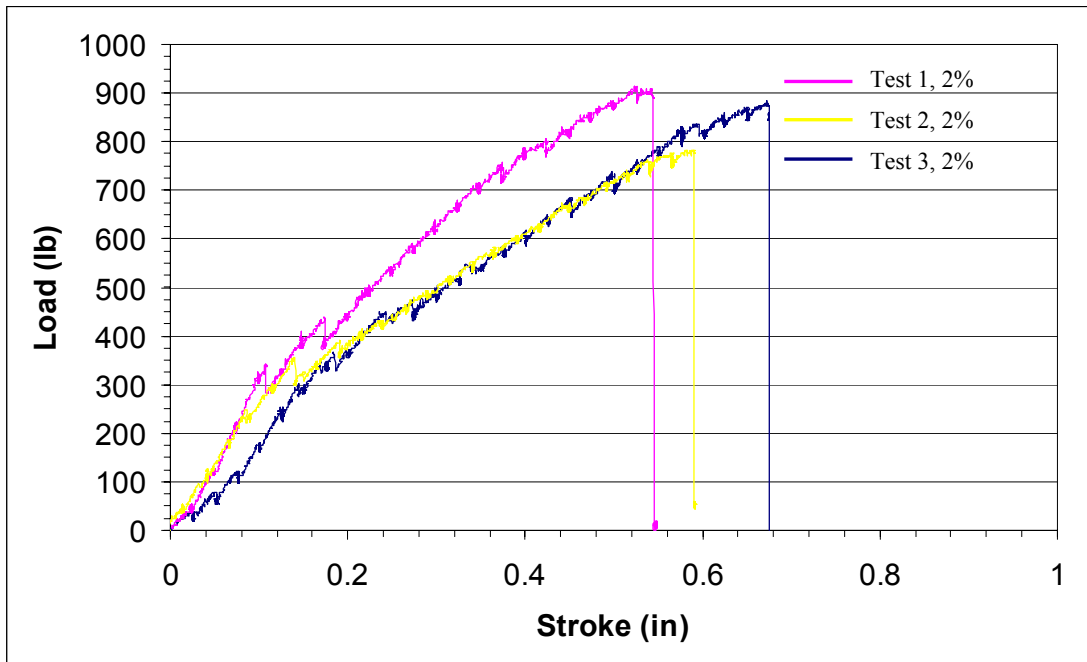


Figure 34. Load-Stroke Response of T-sections (2%, 0.011'')

In Figure 35, both specimens have a similar initial response, although first failure load is higher for Test 1 than Test 2. There is then an increase in load for both specimens until the stroke reaches 0.45 in. After this point, the behaviors of the two tests begin to diverge. For specimen 1, crack growth occurs along the skin-flange interface through the z-pinned region until final failure. But for specimen 2, the crack stops growing along the z-pin region at a stroke of 0.45'', at which point, failure occurred in the outer most skin layer due to tensile failure and delamination, not an expected failure mode.

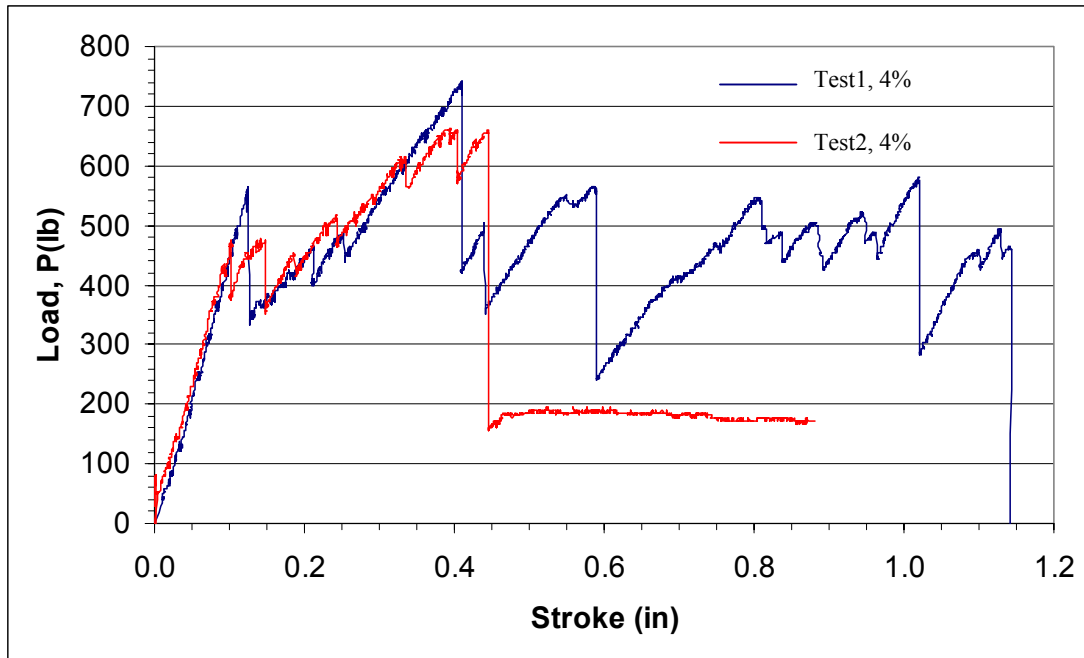


Figure 35. Load-Stroke Response of T-sections (4%, 0.022'')

In all three tests using a 0.011'' pin at 4% areal pin density, failure of the outermost skin layer occurred, similar to what was described above for test 2 in Figure 35. Figure 36 shows that the final failure occurs at a stroke value of 0.5 in, which is similar to the failure displacement for Test 2 in Figure 35 above. Figure 37 is a photograph showing an example of this type of failure.

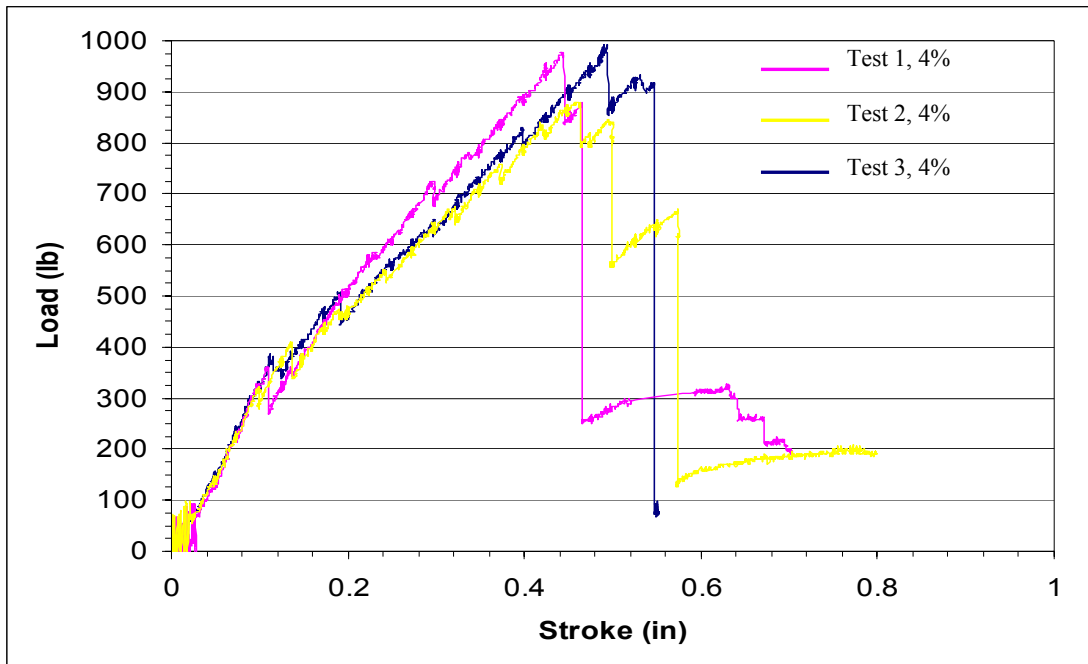


Figure 36. Load-Stroke Response of T-sections (4%, 0.011")

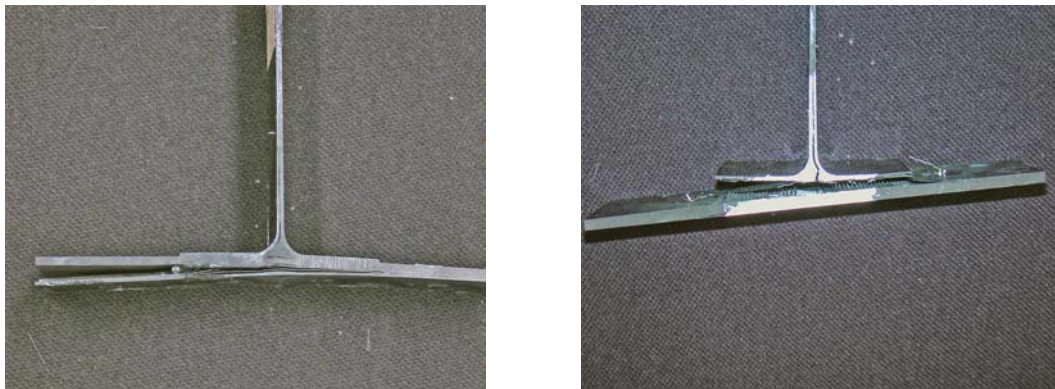


Figure 37. Examples of Fracture in T-Section Tests



Figures 38 and 39 show load vs. strain readings from the T-specimen's web and skin, respectively. As shown in Figure 38, the average slope obtained from the web load-strain readings was 6350 ksi, very close to the axial elastic modulus of 6400 ksi, given in Table 4 above.

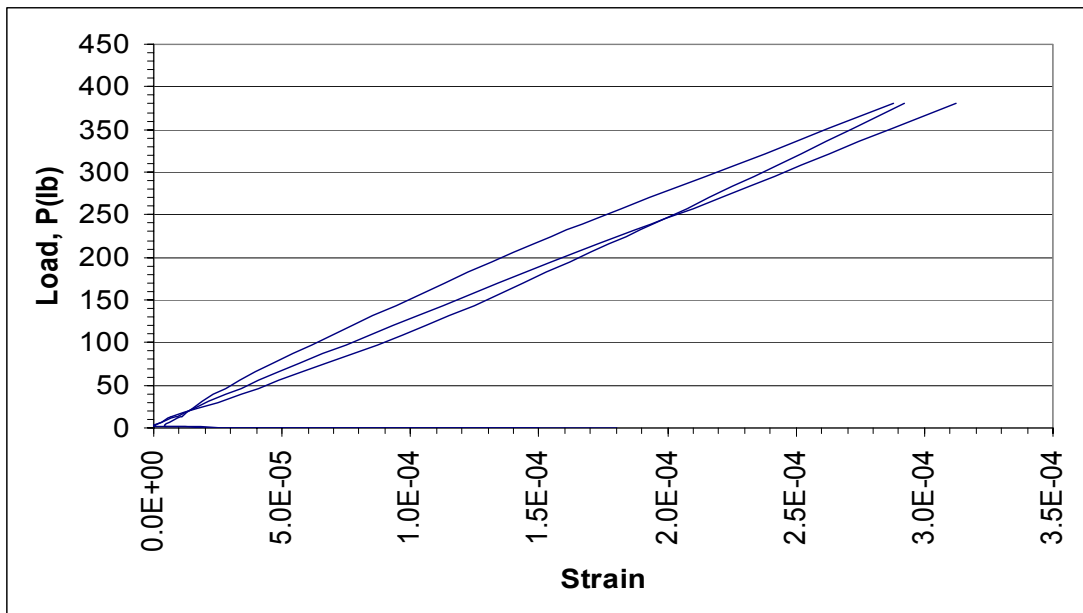


Figure 38. Load-Strain Response of T-Section Web

According to Figure 39, the deformed shape of a T-specimen is symmetric until first failure load. Crack propagation is not symmetric when the crack grows in the z-pin region, as is revealed in the load-strain curves of gages 1-5 and 3-7. The reason for non-symmetric crack growth through the reinforcement is shown below in Figures 40 and 41, which illustrate the different delamination mechanisms in T-sections with and without z-pins.

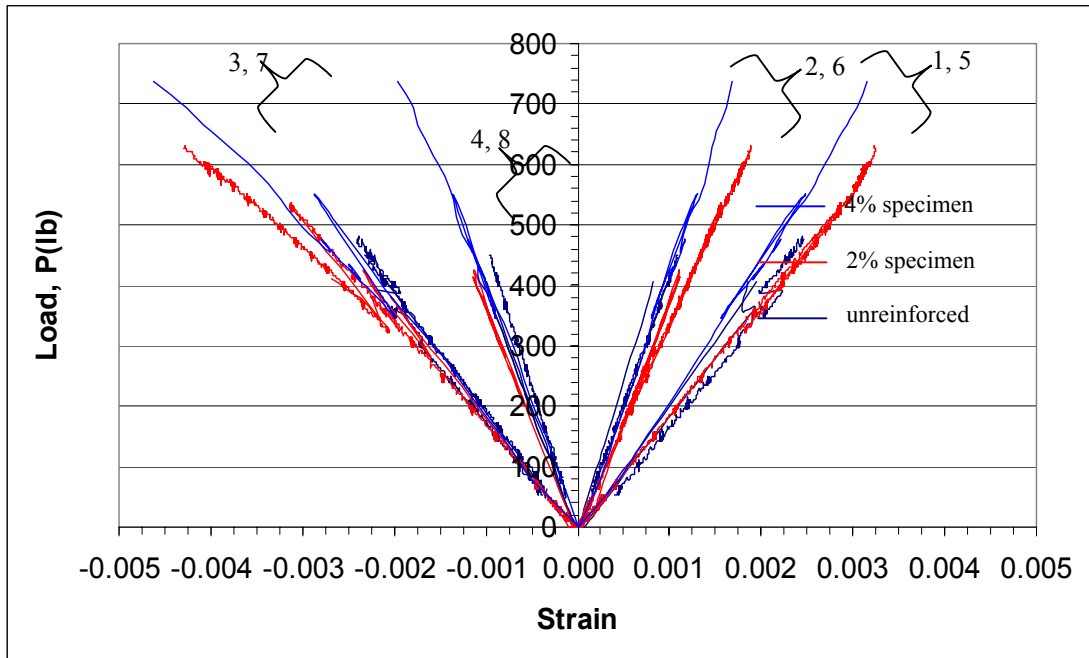


Figure 39. Load-Strain Response of T-section Skins

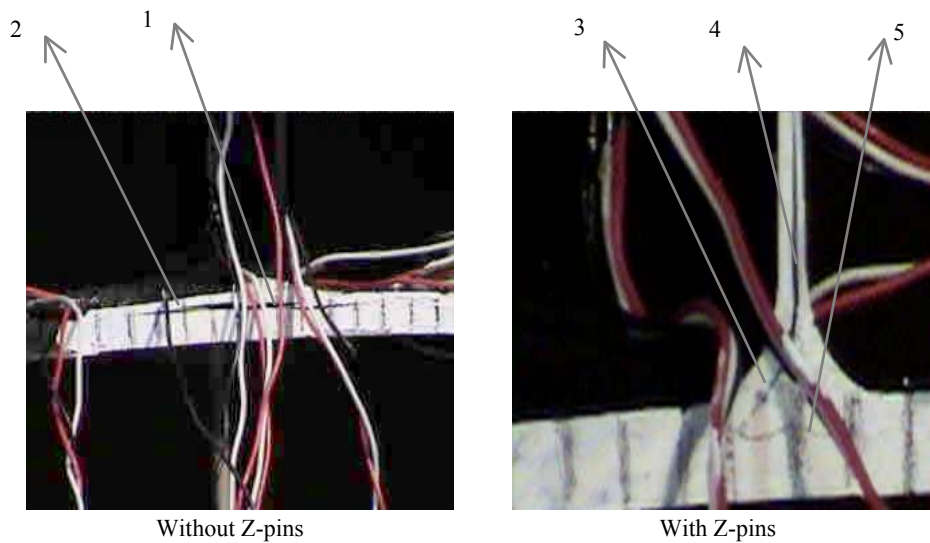


Figure 40. Delamination Mechanisms in T-sections

In T-sections without z-pins the first mechanism, which corresponds to the first failure load in the test data, is the delamination of the skin-web-flange interface at the bottom of the resin rich area (1). The delamination continues to grow towards the tapered ends of the skin-flange interface (2) until the skin and flanges are separated at final failure.

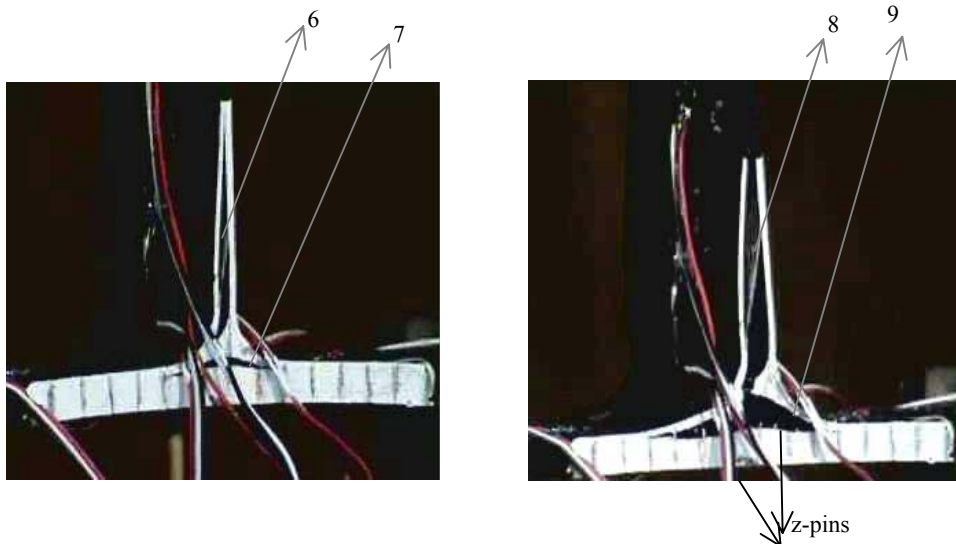


Figure 41. Delamination Growth in T-Section with Z-pins

For the T-sections with z-pins, the first delamination mechanism begins at the resin rich area (3) as in the unreinforced specimen. However, because the z-pins hold the growth along the skin-flange interface, the delamination moves around the resin rich region and begins to climb upward along the mid-plane of the web (4, 6, 8) until it is restrained by the grips at the top.

At this point the delamination progresses along the flange-skin interface (7) until the z-pinned region is reached. When the z-pin row in front of the delamination crack reaches its delamination energy the row fails and the delamination continues to grow along the skin-flange interface toward the tapered-ends (9) as the next z-pin rows reach their delamination energy. This mechanism repeats itself until the final failure of the T-section and is consistent for T-sections with 2% and 4% reinforcement.

## IV. Analytical Study

### DYNA3D Modeling

#### DCB & ENF Specimens.

The DCB and ENF specimens were modeled using 2-D shell elements and broken into two sub-laminates of thickness  $h/2$  with nodes located at the mid-surface of each sub-laminate. For computational efficiency, a half model is used. Cohesive elements are placed along the connection plane, or the mid-surface between the two sub-laminates. The number of cohesive elements used depends upon the number of shell elements on the top and bottom laminas. A fine mesh is used in the region beginning immediately after the initial crack and continuing to the end of the z-pinned region. A more coarse mesh is used for the initial crack and the region following the z-pins. Figure 42 illustrates the DCB/ENF model.

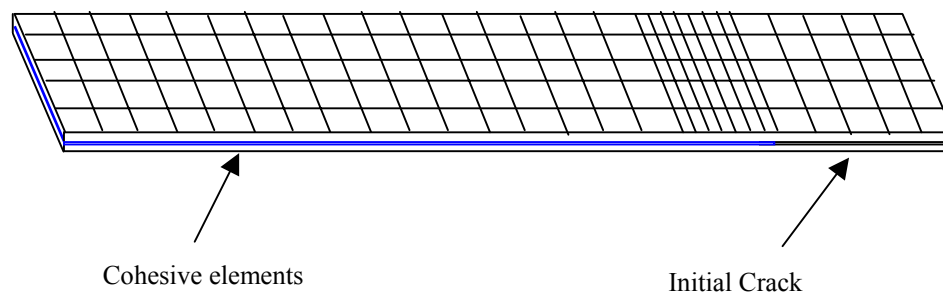


Figure 42. Schematic of DCB/ENF Modeling in DYNA3D

The displacement velocity is slowly ramped to eliminate any stress wave development. Nodal forces where the load is applied are calculated by DYNA3D and are output into a text file as a time history. Crack opening displacement data can be obtained from a binary output file and can be converted to a text file if required. The internal damage variable,  $d$ , described in Chapter II, is used to track crack propagation along the cohesive elements. The time history for the damage variable can be output at any time either during or after the analysis. For an undamaged cohesive element the value of damage parameter is 1; as the cohesive element fails and the crack propagates to the next element the damage parameter reduces to zero. Thus all vital parameters: COD, failure load and crack tip location can be easily calculated using DYNA3D analysis. Input files are rapidly generated using the software. Post-processing the results from the binary and the text output files generated by DYNA3D is accomplished using both Ls-Post/Taurus, which is capable of reading the binary output files, and the *FORTTRAN* codes developed by ASRI which rapidly plot vital parameters in the desired fashion.

For DCB specimens, a large initial load is required to break the blunt crack that exists at the end of the Teflon separation tape, as explained in Chapter III. Thus for modeling purposes, it is not feasible to use a single cohesive zone model to represent both the very initial crack and the crack propagation region.

Relatively high values were used for the initial stiffness and delamination energy on the first row of cohesive elements just ahead of the initial blunt crack. Once this row of elements fails, the following cohesive zone elements have uniform parameters deduced from the experimental results. Figure 43 shows a representative DYNA3D mesh used in the analysis. In ENF specimens a knife was used to open the blunt crack, therefore there is no need for two stiffness regions and both are given the same value.

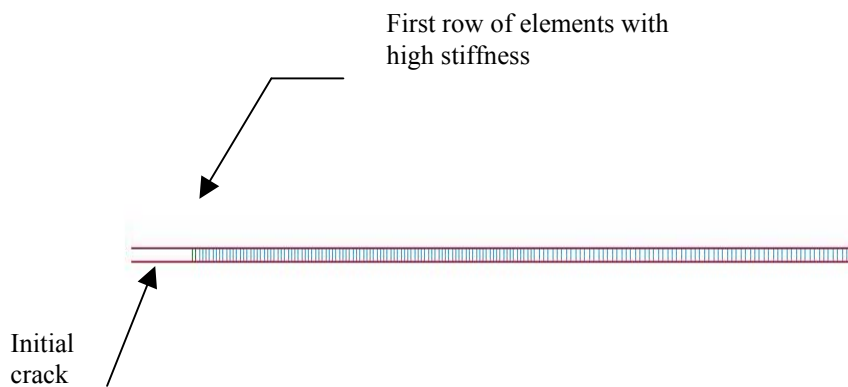


Figure 43. DYNA3D Mesh for DCB Simulation

### T-Section Specimens.

At the time of testing, the reinforced and un-reinforced T-section modeling program was non-functioning. The nature of the problem was not clear and due to time constraints no T-section models were created.

## Analytical/Experimental Comparison

### Unreinforced DCB Specimens.

Convergence studies were performed to determine the mesh size needed to maximize accuracy and minimize the time required to complete the simulation. A total of 183 elements along the length were used to model each sub-laminate. Varying the number of elements along the width did not affect the analysis accuracy significantly and for this analysis two was used, thus a total of 366 cohesive elements were present in the model. The physical and geometric properties of the specimens are shown in Table 7. The properties of both cohesive zones, the blunt crack region and the crack propagation region are given in Table 8. Comparisons of the experimental and analytical results are plotted in Figures 44 and 45.

Table 7. DCB Geometry and Physical Properties

---

Dimensions of specimen 8.75 x 1 x 0.14 inches		
Initial crack length 0.75		
$E_{11} = 17.3 \times 10^6$ psi	$E_{22} = 1.38 \times 10^6$ psi	$E_{33} = 1.38 \times 10^6$ psi
$G_{12} = 6.09 \times 10^5$ psi	$G_{23} = 4.76 \times 10^5$ psi	$G_{13} = 6.09 \times 10^5$ psi
$\nu_{12} = 0.3$	$\nu_{13} = 0.3$	$\nu_{23} = 0.45$

---



Table 8. Cohesive Zone Property for the Analytical Model

Property			Crack Initiation	Crack Propagation
Stiffness	$K_I$	psi	$1.95 \times 10^7$	$1.95 \times 10^{10}$
Critical Stress	$S_{Icr}$	psi	2900.75	2900.75
Energy Release Rate	G	lb/in	1.425	0.456

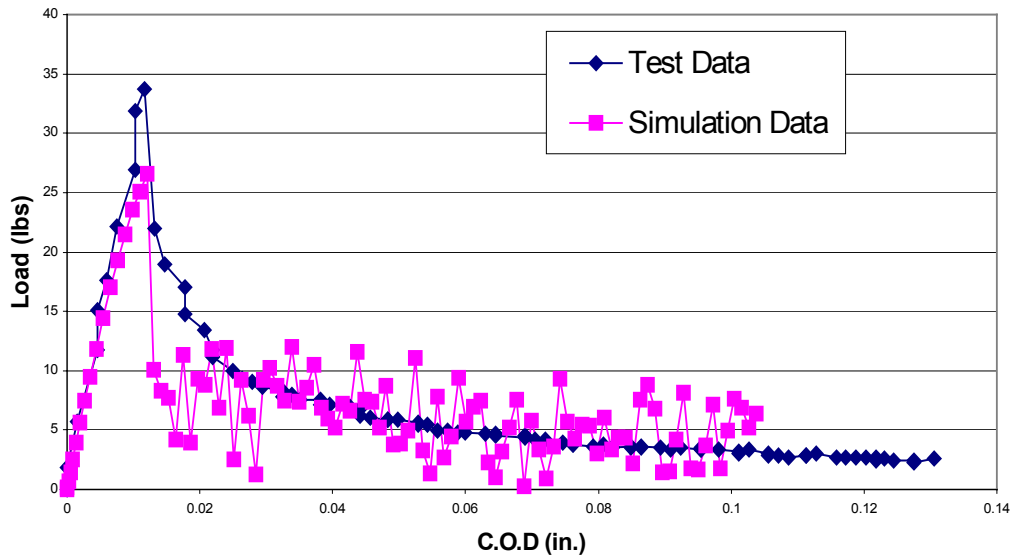


Figure 44. Unreinforced Specimen Comparison (Load vs. COD)

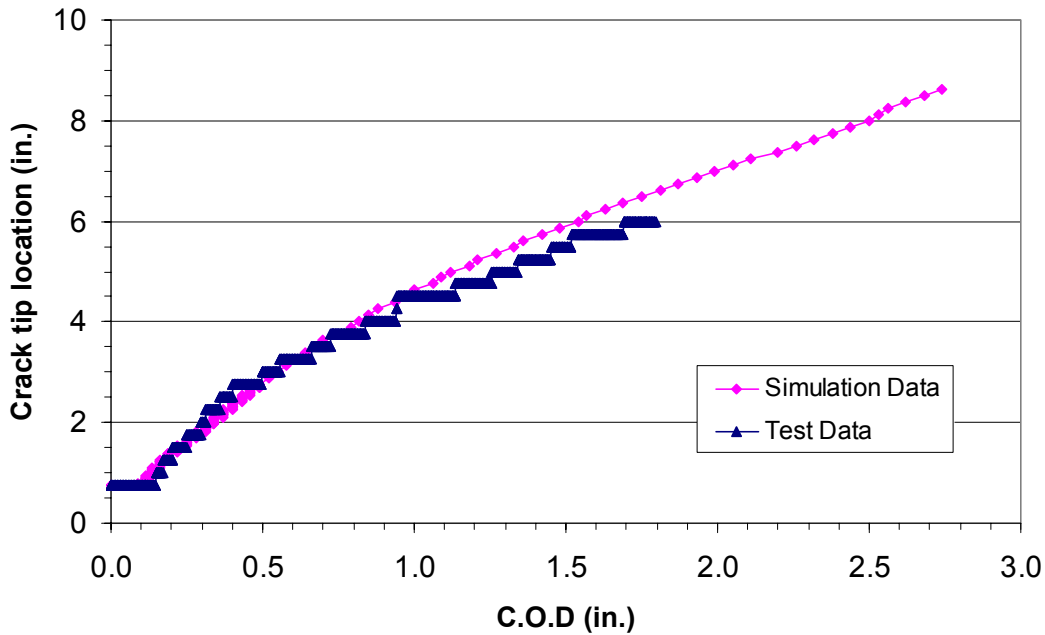


Figure 45. Unreinforced Specimen Comparison (CTL vs. COD)

As seen in the figures, there is a good correlation between the experimental results and the DYNA3D model. In Figure 44, some dynamic instability in the numerical results is visible; this can be attributed to the fact that the density and time step were scaled to enable DYNA3D to complete the analysis in a reasonable time frame. Because DYNA3D is a transient dynamic code, low crosshead displacement rates must be used to run static analyses. However, since the crosshead rate directly affects simulation time a trade-off is made. Hence, dynamic effects can be minimized, but it is unrealistic to expect to eliminate them altogether.

### Z-Pinned DCB Specimens.

For z-pinned DCB specimens, a half model with 2 elements along the width and a total of 212 elements along the length were used resulting in 424 total cohesive elements. Figure 46 shows the mesh for a representative analytical model.

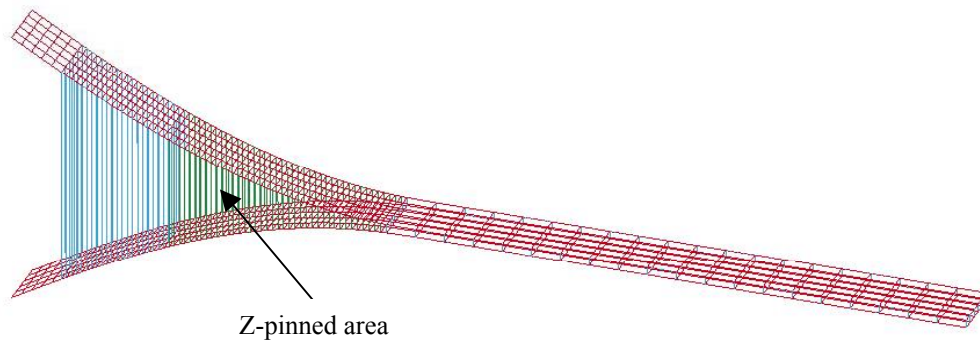


Figure 46. DYNA3D Mesh for Z-pinned DCB Simulation

A quasi-static analysis method was again used, during which the velocity was slowly ramped to eliminate any transient effects. Velocity was applied at the end nodes allowing the crack to propagate along the length of the specimen.

Z-pinned DCB test results are plotted for A, E, G and H type specimens. The same prepreg material used to fabricate un-reinforced specimens was used for the z-pinned specimens, thus the properties given in Table 7 are used here. In addition, the energy release rate in the un-reinforced region of the z-pinned specimens is same as that of the entire un-reinforced specimen.

Several steps were performed to determine the delamination property to be used in the simulation for the reinforced region. First,  $G_I$  was calculated manually via the area method. Next, the test data was curve fit using equations from beam theory resulting in another  $G_I$  value that was compared to the value calculated manually. Figure 47 shows a comparison between the experimental test data from an H-type DCB specimen and the curve fit developed from beam theory. Similar plots for A, E, and G type specimens can be found in Appendix A.

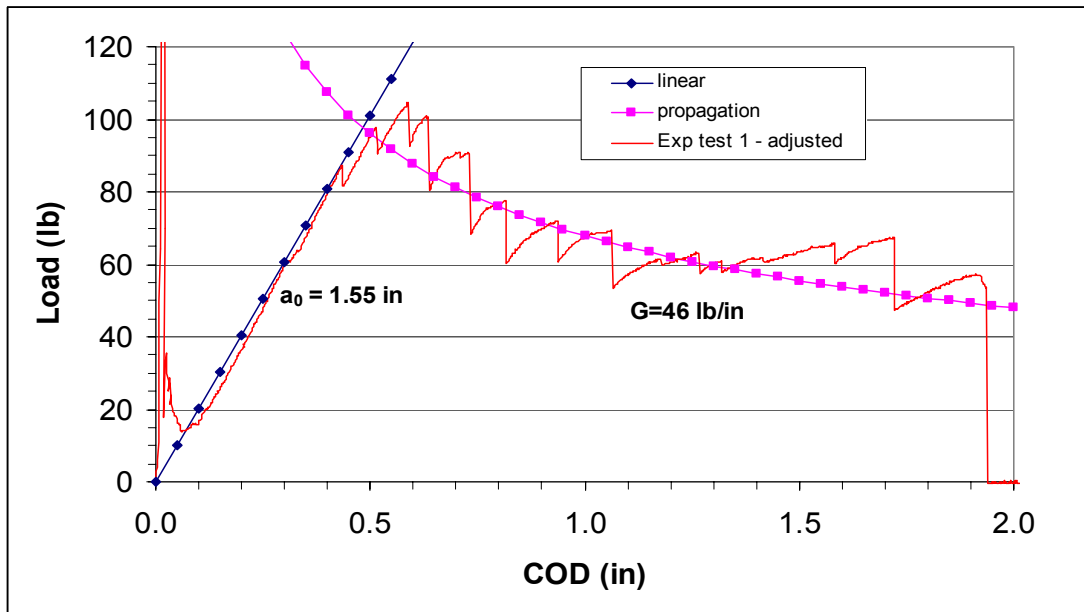


Figure 47. Curve-fitting to Calculate  $G_I$

The curve fitting relations for the linear and propagation regions of Figure 47 are:

$$P_L = \frac{3 \Delta E I}{2 a_0^3} \quad (5.1)$$

and

$$P_P = \frac{\left( G^3 E B^4 h^3 / 27 \right)^{1/4}}{\Delta^{1/2}} \quad (5.2)$$

Where  $P_i$ ,  $G$ ,  $\Delta$ ,  $E$ ,  $B$ ,  $h$ ,  $I$ , and  $a_0$  are load, Mode I strain energy release rate, crack opening displacement, elastic modulus, width, specimen half thickness, moment of inertia, and initial crack length.

The elastic modulus of the z-pinned region, like the energy release rate, is not a material property in the z-pinned region, but is rather a structural property. Thus, in the linear region, Equation (5.1),  $E$  is treated as an independent variable, the value of which was chosen to match the slope of the curve fit to that of the experimental data. For specimens with reinforcement densities of 2% and 4%, this assumes a longitudinal modulus 90% to 110% of the original value listed in Table 7. In the Steeves and Fleck analysis (9) tests were performed using specimens reinforced with 0.011” diameter pins at a 2% areal density their result matches well with those found in the present analysis.

The stiffness value obtained from the curve fit was then entered into Equation (5.2), from which  $G_I$  was obtained. Table 9 lists the z-pin region property obtained from this process for each specimen type.

Table 9. Cohesive Zone Property in the Z-pin Region

<b>Smeared Property</b>			<b>A</b>	<b>E</b>	<b>G</b>	<b>H</b>
Stiffness	$E_{11}$	Msi	15.6	17.3	17.3	15.6
Critical Stress	$S_{Icr}$	ksi	1.3	1.3	1.3	1.3
Energy Release Rate	$G_{Ic}$	lb/in	45	50	38	46

Figures 48 and 49 show comparisons of the experimental and analytical results for an A-type specimen. The reader will notice good agreement in the linear region up to peak load, but only fair agreement in the propagation region as the model overestimates the failure COD and the load throughout the region. Because the deviation occurs only in the propagation region, the error is due to an exaggerated  $G_{Ic}$  value.

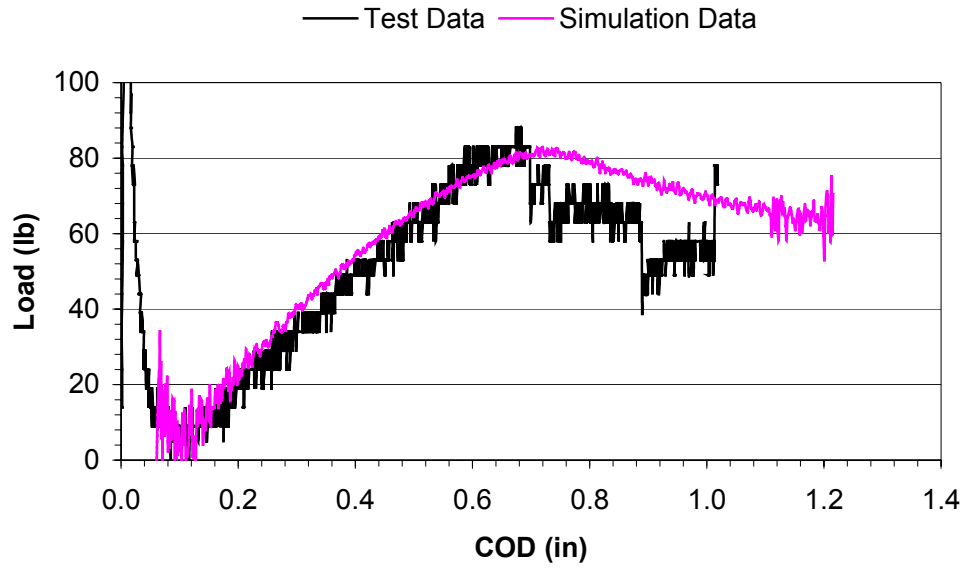


Figure 48. Load vs. COD Comparison (A-type,  $G_{Ic} = 50$  lb/in)

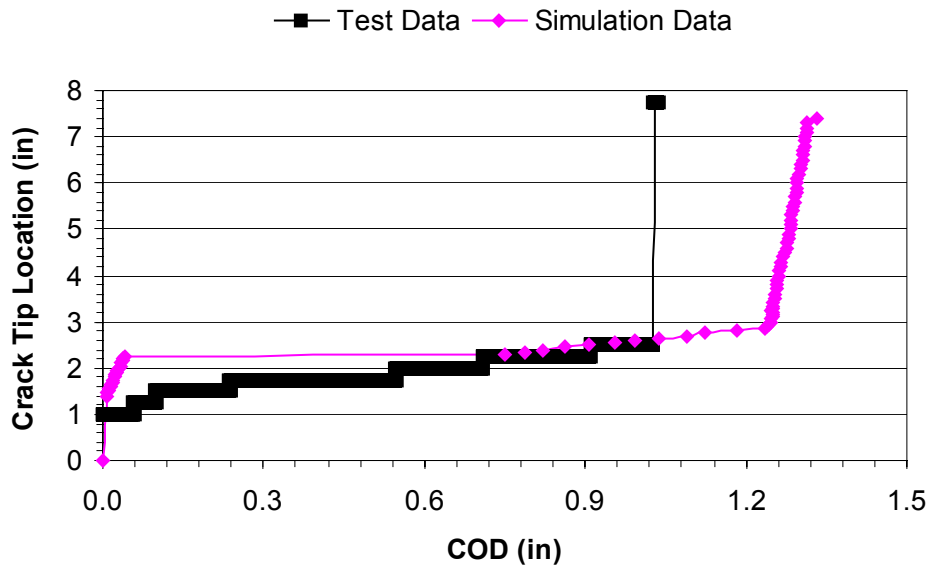


Figure 49. CTL vs. COD Comparison (A-type,  $G_{Ic} = 50$  lb/in)

A second attempt to model the A-type specimen was made with  $G_{Ic}$  reduced to 40 lb/in. The results are shown in Figures 50 and 51, agreement is greatly improved.

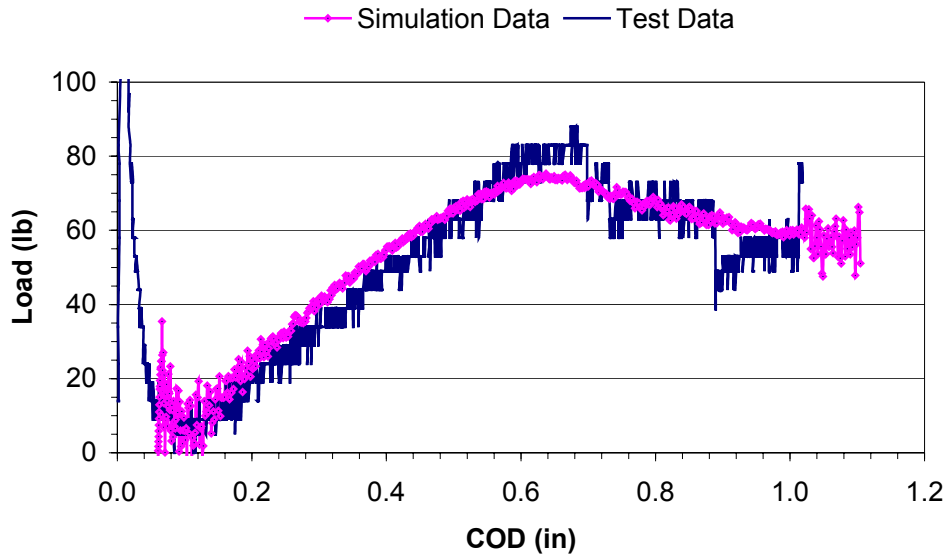


Figure 50. Load vs. COD Comparison (A-type,  $G_{Ic} = 40$  lb/in)

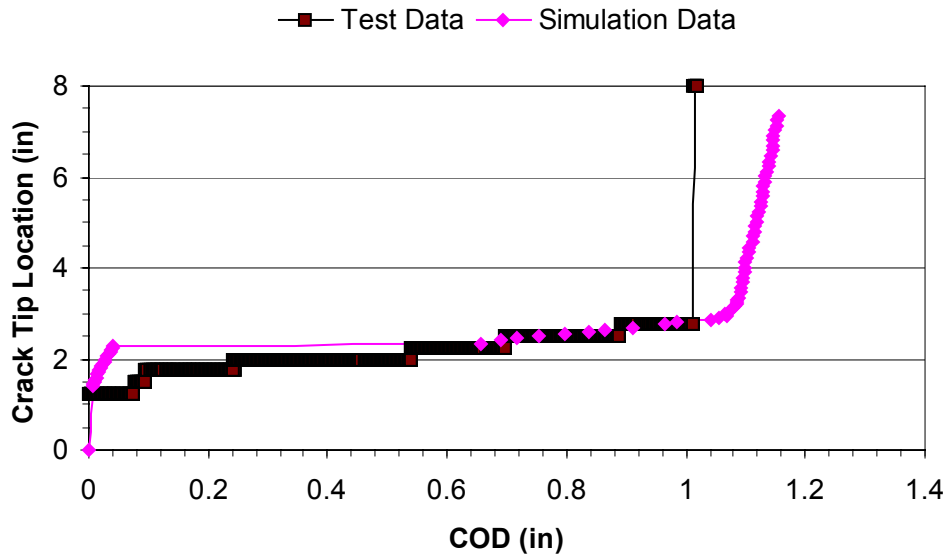


Figure 51. CTL vs. COD Comparison (A-type,  $G_{Ic} = 40$  lb/in)



Figures 52 - 55 illustrate the comparisons for E and H-type specimens using  $G_{Ic}$  values determined from the curve fit presented in Table 9. The simulations produced results that agreed very well with the experimental data.

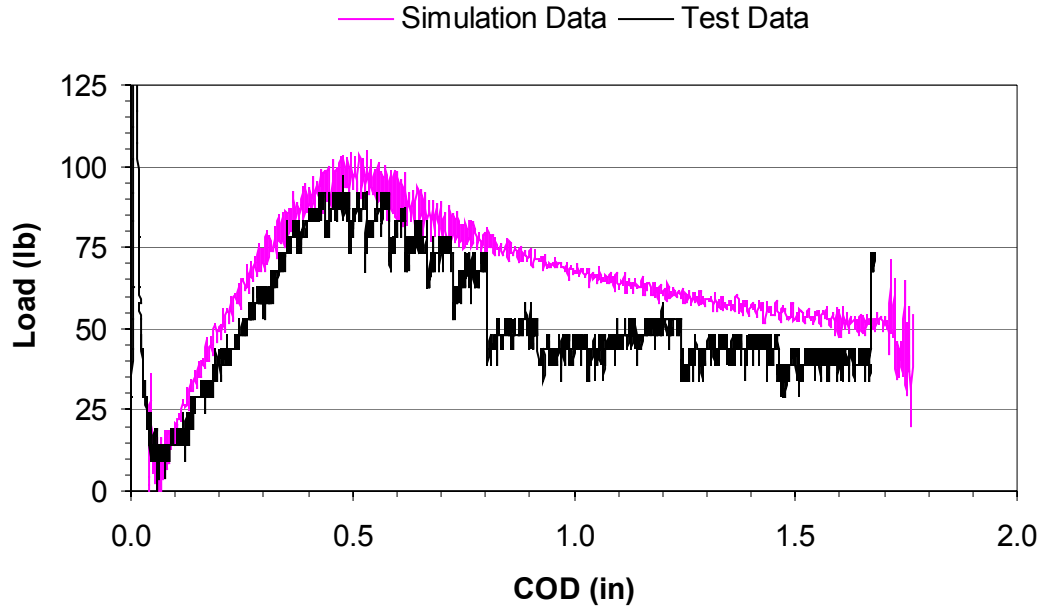


Figure 52. Load vs. COD Comparison (E-type,  $G_{Ic} = 50$  lb/in)

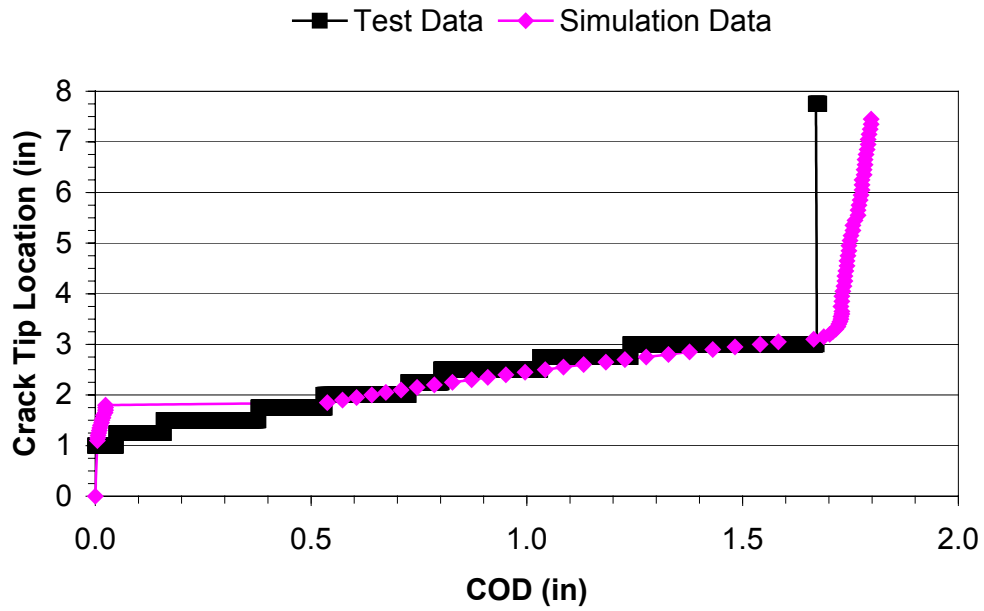


Figure 53. CTL vs. COD Comparison (E-type,  $G_{Ic} = 50$  lb/in)

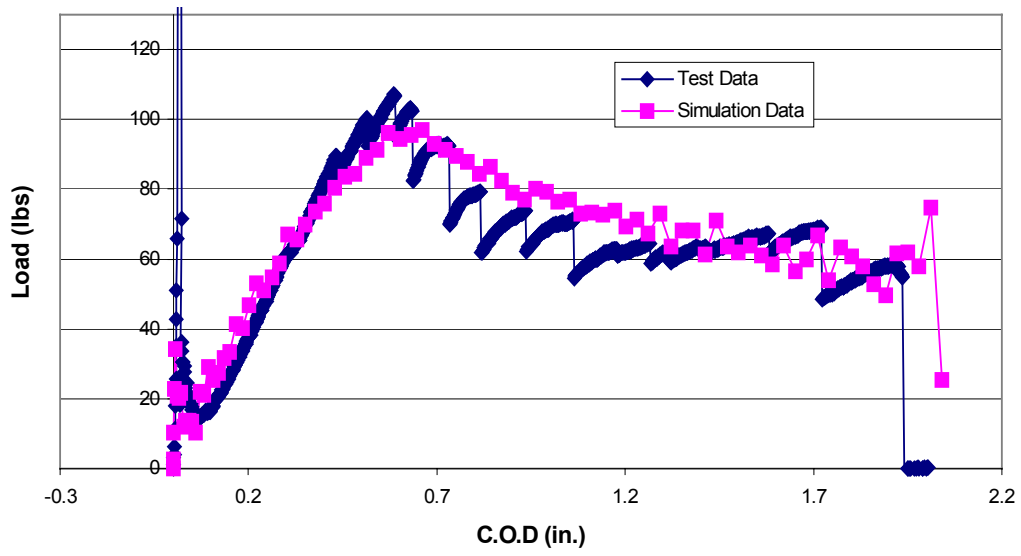


Figure 54. Load vs. COD Comparison (H-Type,  $G_{Ic} = 46$  lb/in)

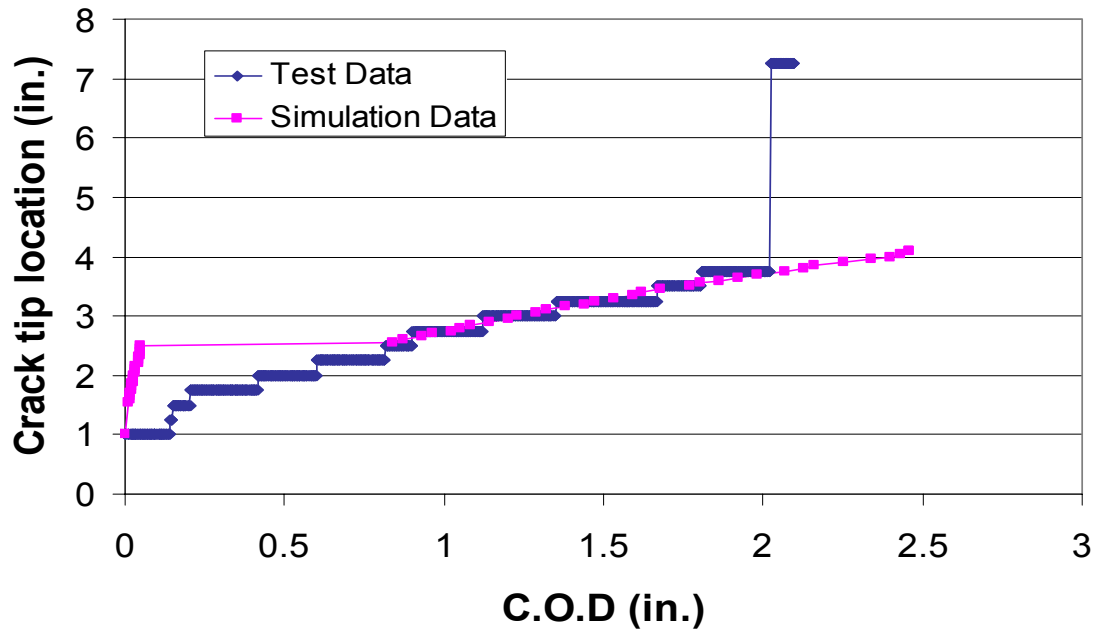


Figure 55. CTL vs. COD Comparison (H-Type,  $G_{Ic} = 46$  lb/in)

Unreinforced ENF Specimens.

The physical and geometrical properties of ENF specimens are shown in Table 10 while the properties of the cohesive zone are given in Table 11. In ENF testing there is no blunt crack to overcome, since the crack opened using a knife to bypass the blunt crack. Table 11, therefore, presents data only for the propagation region of the test.

Table 10. ENF Specimen Geometry and Physical Properties

---

Dimensions of specimen: 5.65 x 1 x 0.14 inches

Initial crack length: 0.5 in.

$$E_{11} = 1.28 \times 10^7 \text{ lbs/in}^2$$

$$\nu_{12} = 0.33$$

---

Table 11. Cohesive Zone Properties for ENF Model

<b>Property</b>	<b>Crack Propagation</b>		
Stiffness	$K_{II}$	psi	$2.0 \times 10^7$
Critical Stress	$S_{IIcr}$	psi	16000
Energy Release Rate	$G_{IIc}$	lb/in	10.0

Modeling of un-reinforced ENF specimens was accomplished by applying a three-point bend load to the DCB model described previously. Consequently, the physical properties and mesh size used to model un-reinforced ENF specimens are the same as that of the un-reinforced DCB specimen.

The experimental and the analytical results are shown in Figures 56. They show very good correlation up to the failure point, where dynamic effects dominate.

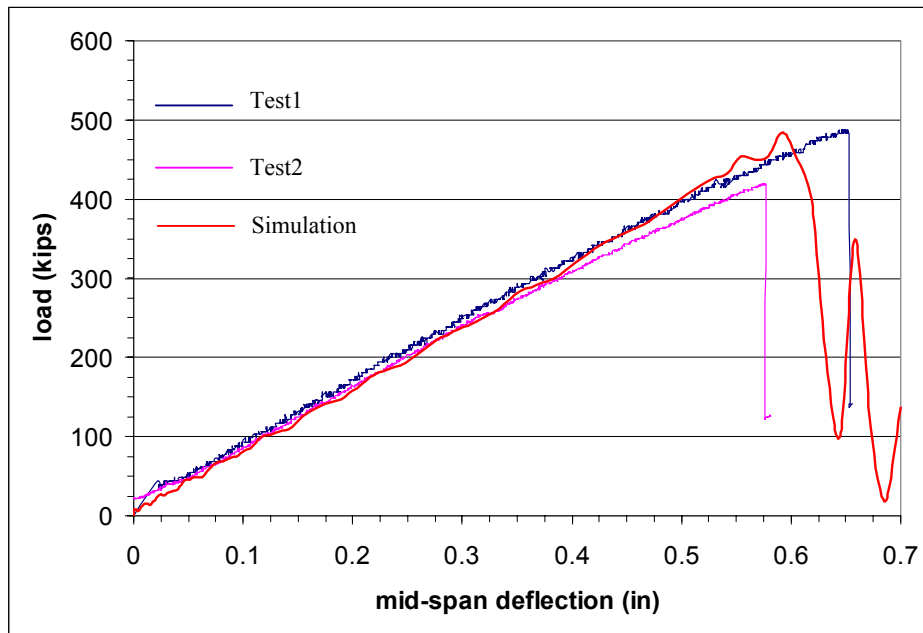


Figure 56. Comparison for Unreinforced ENF Specimen

#### Z-pinned ENF Specimens.

Because of the lack of crack growth, no useful fracture data could be drawn from the reinforced ENF tests. Therefore, no simulations were performed on z-pinned ENF specimens.

## **V. Results and Discussion**

### **Review**

Numerous tests have been performed on DCB, ENF, and T-sections with third directional reinforcement. The management of these tests has provided consistent patterns in material and component properties. The effect of z-pins, percentage of z-pin reinforcement, diameter of z-pin and area of reinforcement have been explored using DCB and ENF specimens. Moreover, the delamination behavior of through-thickness reinforcement composite T-sections with z-pins was investigated under three-point bending load at room temperature.

The computational work in this research focused on validation of analytical models for z-pinned DCB and ENF specimens and T-stiffeners under static loading. Cohesive delamination elements have been implemented in finite element models using elastic-plastic smeared properties to model the z-pinned region. Cohesive element formulation in DYNA3D was used for FE analyses using shell elements. Predictions from the performed analyses using the computational models validate test results and provide a complete picture of the component's response.

## Results

### Effect of Z-pin Diameter and Areal Density.

#### DCB Specimens.

Figure 57 is a load vs. COD comparison of an un-reinforced DCB specimen to E, F, G, and H-type z-pinned specimens, each of which has a 1" x 2" reinforcement area.

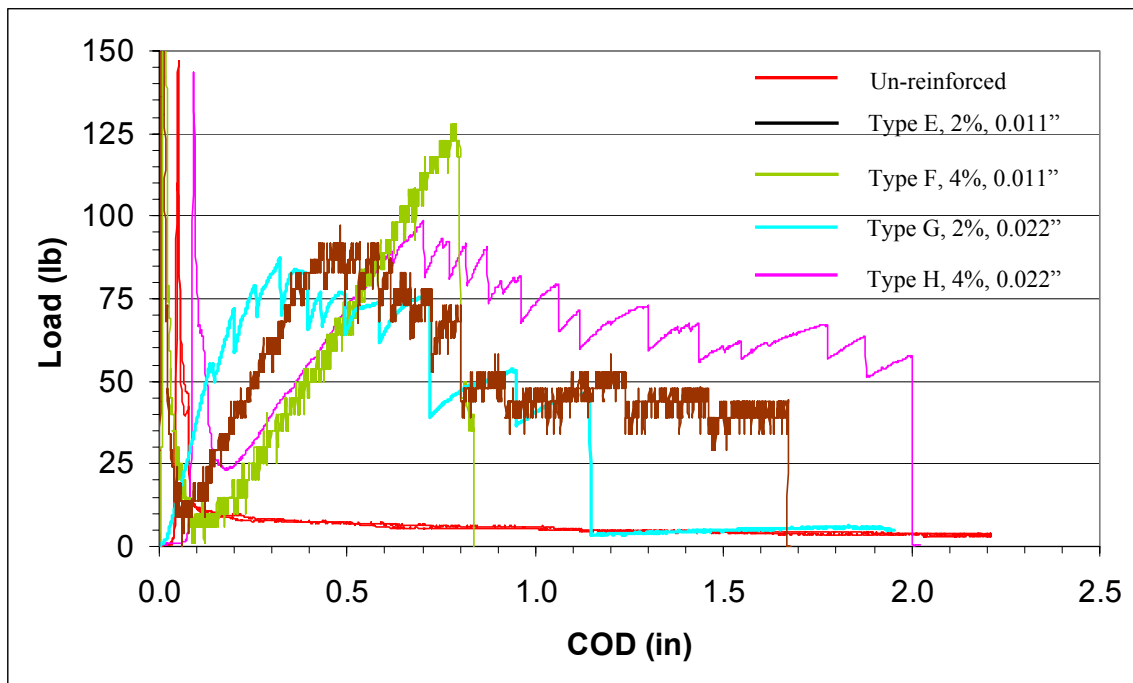


Figure 57. Comparison of DCB Specimens (Load vs. COD)

The load vs. COD response of z-pinned specimens mirrors that of the un-reinforced DCB specimen before the crack reaches the z-pinned region. As the crack encounters the first row of z-pins, the mode I energy increases until the

ultimate load is reached, at which point the first z-pin row fails. Z-pinning in DCB specimens resulted in a 500% - 830% increase in the ultimate load and a 250% - 550% increase in the overall mode I failure energy. The progression in ultimate load and total energy consumed from the G-type specimen to the F-type specimen reflects a progression in the amount of z-pin surface area in contact with the surrounding matrix.

In mode I, the response of z-pinned laminates is almost completely determined by the frictional contact area, however, for other loading situations, this is not the case, as will be seen. Table 12 lists the peak load, pin density and contacting surface area per inch of laminate for each specimen type.

Table 12. Comparative Data in Z-pinned DCB Specimens

	0.022" Diameter		0.011"Diameter	
	G (2%)	H (4%)	E (2%)	F (4%)
Pin Density (Pins/In <sup>2</sup> )	52.5	105	210	420
Surface Area (In <sup>2</sup> /In)	0.544	1.088	1.088	2.176
Peak Load (lbs)	75	100	100	125

An important consequence of this result can be understood by comparing the curves of the H and E-type specimens in Figure 57. Both specimen types have the same contact area and, not surprisingly, both curves traverse the same path, although clearly shifted by a COD of 0.3 inches. The important distinction between the two is difference in the areal/volume and actual pin densities. As



defined in Chapter III, areal/volume density is the ratio of the total cross sectional area/volume of every z-pin inserted into a laminate to the area/volume in which the z-pins were inserted. Actual pin density is simply the number of pins inserted in a given area/volume. From Table 12, E-type specimens have an actual pin density twice that of an H-type specimen, while H-type specimens have an areal/volume density twice that of an E-type specimen.

The result suggests that should a designer wish to strengthen a composite structural member by raising the load required for mode I crack propagation from 25 lbs (that of an un-reinforced DCB specimen) to 100 lbs, the option exists of using fewer, large pins that will occupy a large volume of laminate or many smaller pins that will occupy a small volume of laminate. Computational results by Grassi et. al. (24) determined that the minimum pin diameter should be used in order to minimize laminate fiber misalignment and micro-buckling. Fiber misalignment was shown to be a critical factor in reducing the laminate's strength and stiffness, especially in compression. Therefore, in a choice between E and H-type specimens, it would be imprudent to use the H-type large diameter pin especially at a high areal/volume density. Although no research has currently been done to study the effect that varying z-pin areal/volume density while maintaining a constant pin diameter has on a laminate's in-plane properties, there

is no reason to believe that inserting more pins would not cause more fiber misalignment and a more adverse overall effect on the laminate.

It is worth mentioning that all z-pinned composite research done up to the time of this report's writing has involved 0.011" and 0.022" diameter pins, so it is not known how small of a reinforcing pin may be used to promote increases in the mode I fracture toughness and still not fail in an unexpected manner.

While z-pinning provides a large increase in the peak load reached during testing, the primary benefit of reinforcement is damage tolerance in the form of reduced crack length and crack opening. Figure 58 illustrates the load vs. crack tip location for un-reinforced and z-pinned DCB specimens, each has a 1" X 2" reinforcement area. As seen in the figure the load required to propagate the crack throughout the un-reinforced specimen decreases throughout the test, while in the reinforced specimens higher loads are required for the crack to enter and propagate the z-pinned region.

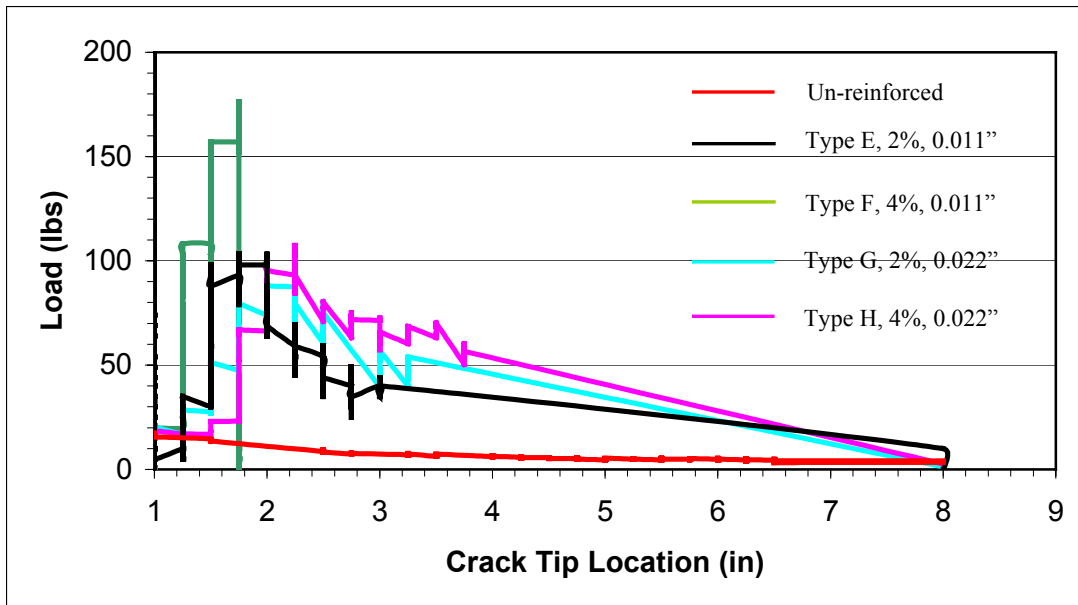


Figure 58. Comparison of Load vs. CTL in DCB Specimens

This is useful in two ways: To ensure that a crack does not propagate more than 2 inches, for instance, this chart gives a design load not to exceed. On the other hand if a load is specified, the chart can be used to design a z-pin configuration capable of handling the load without allowing extensive delamination.

Figure 59 illustrates the crack tip location vs. crack opening displacement behavior of z-pinned and un-reinforced DCB specimens. Crack propagation in each of the reinforced specimens is similar although there is clearly a progression in the COD to failure from the G-type specimen to the H-type specimen. The figure indicates that once the crack reaches two inches in length, or the location where the z-pinned region begins in reinforced specimens; its length is reduced or

restrained by the z-pins. As the tests progress, the gap in crack length widens slightly until final failure. A progression in the crack length gap from the G-type to the H-type specimens is shown in Figure 59. Although, the F-type tests were incomplete, it is evident in the figure that the crack length gap is greatest for this specimen type.

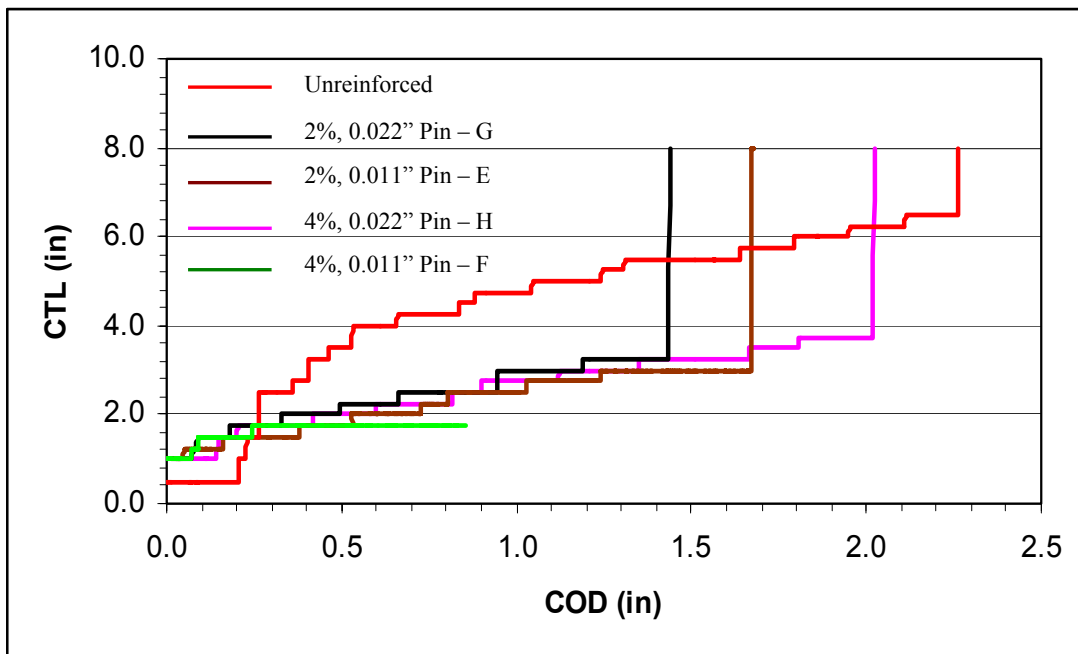


Figure 59. COD vs. CTL Comparison of DCB Specimen Tests

### T-Section Specimens.

Figure 60 shows a comparison of an un-reinforced T-section specimen and representative specimens from each reinforced T-section configuration. Since T-section specimens are reinforced with pins of the same diameter and areal

densities as the DCB specimens, the actual pin densities and relative jumps in contact surface listed in Table 12 above apply here.

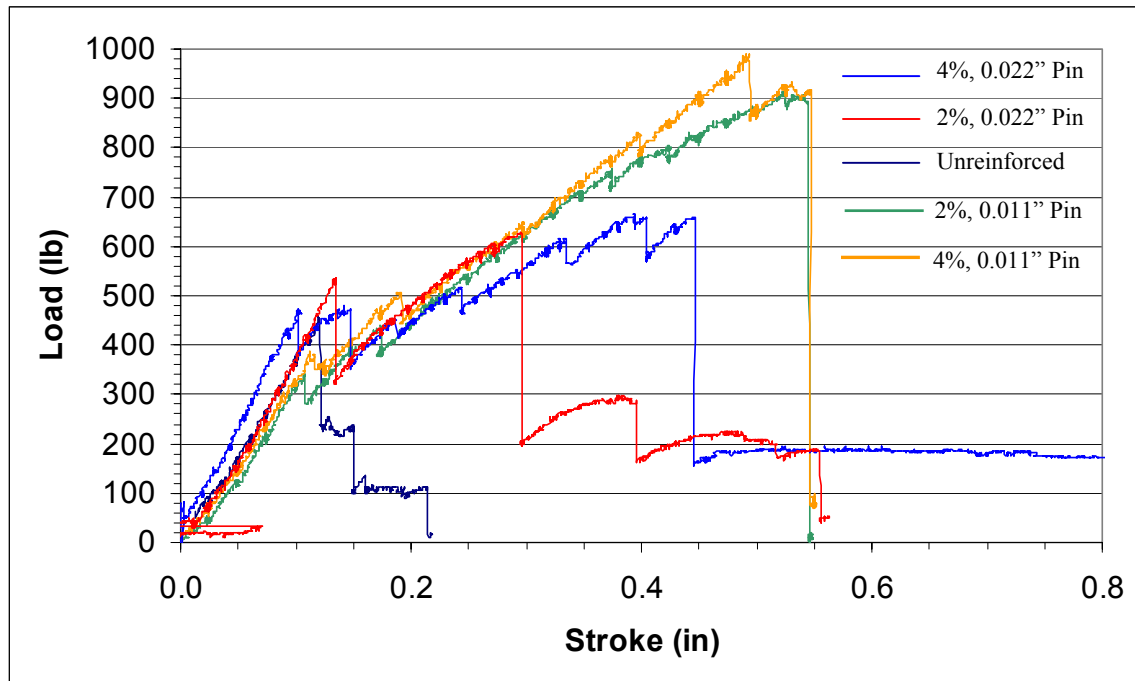


Figure 60. Comparison of T-specimens (Load vs. COD)

Figure 60 illustrates that the reinforced and un-reinforced specimens share the same load-stroke response until the initial drop in load at a stroke of approximately 0.125 inches. This initial load drop corresponds to the delamination occurring at the resin rich region in the center of the t-section. As the tests progress, the response of the un-reinforced specimen deviates significantly while the four reinforced specimens continue to follow a similar path up to their respective failures.

It is difficult to compare the data obtained from reinforced T-specimen testing and reach any meaningful conclusions because: 1) tests of t-section specimens reinforced with 0.022” diameter pins resulted in curves that are highly inconsistent and 2) because of the unexpected skin laminate failures that occurred in many of the 4% specimen tests. What is clear is that the addition of z-pins is effective in halting delamination progress between the skin and flange laminates to the point that the overall failure of the structure becomes the dominant failure mechanism. As evidenced by Figure 60, deformation at failure was more than doubled and ultimate load was increased by 33% - 225%. Further, the total energy required for failure rose by 530% - 1200%.

T-section testing involves modes I and II, but it is unclear to what extent either mode determines the specimen’s response during the test. In its undeformed state, the web and skin laminates are at right angles from the other and therefore initially mode I is dominant. As testing progresses and the specimen deforms, the flange-skin interface rotates, as shown below in Figure 61, and the mode II contribution increases. However, because of crack propagation and opening of the web, this rotation is reduced. Inspection of t-specimens after testing revealed irregular regions in which z-pins appeared to have failed by either the pull-out or internal shear mechanisms described by Cartie et. al. and displayed

in Figure 5. A photograph of a fractured t-specimen revealing the failed z-pins is shown in Figure 62.

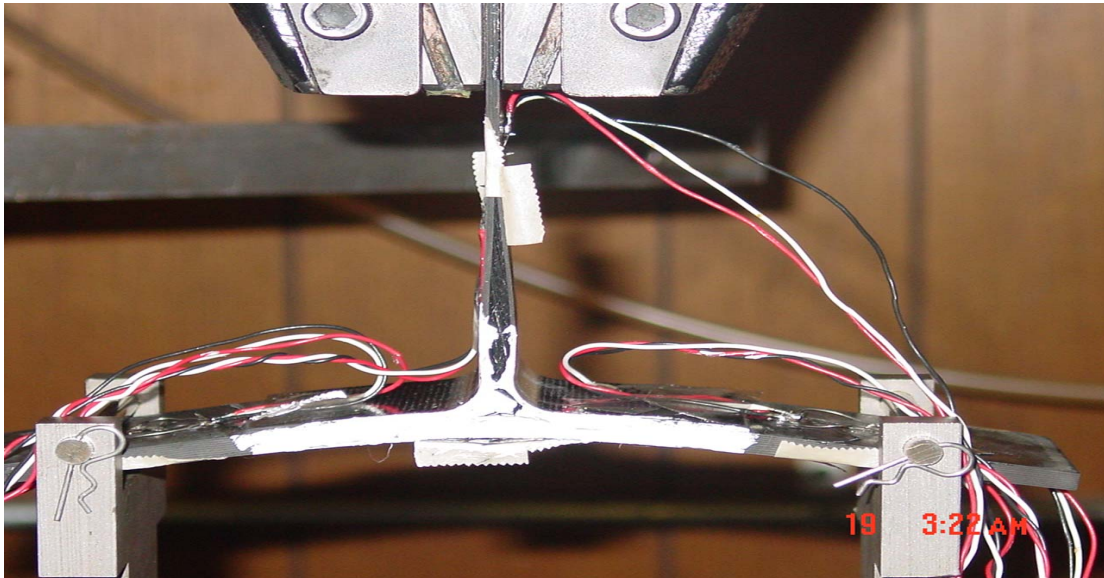


Figure 61. Deformed Shape of T-Section Specimens

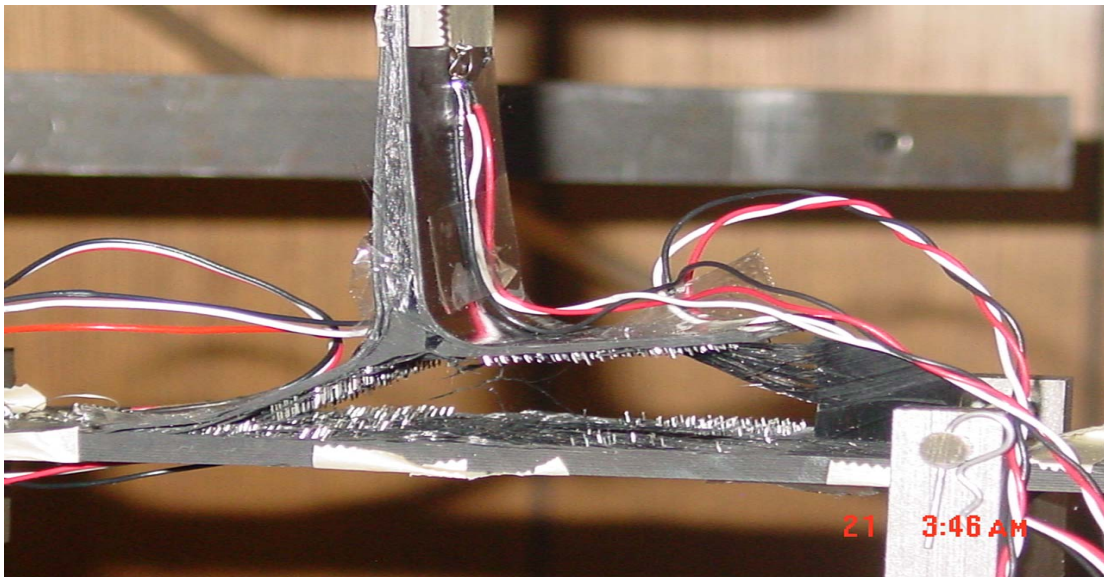


Figure 62. T-Specimen After Testing Showing Z-pins

Rugg et. al. (25), performed tests on t-sections reinforced with 0.022” diameter pins at 2% and 4% area/volume densities using a similar test set up as was described in Chapter III. In (25), equations developed from beam theory are presented to predict the combined energy release rate as well as the  $G_{Ic}/G_{IIc}$  ratio. However, the applicability of the results produced by Rugg is questionable due to significant differences that exist between the test specimens and the fracture mechanisms which Rugg describes.

Important differences include: the use of two support width configurations, narrow (100.8 mm/3.97 in) and wide (152 mm/5.98 in), the lay-up and thickness of the web and skin laminates, (web: 2.2 mm/.086 in, [45/0/45/45/0/45]<sub>s</sub> and skin: 2.3 mm/.905 in, 45/0/0/45/0/45/0/45/0/0/45) and the specimen width, 18 mm/.709 in.

Further, Rugg describes a failure mechanism not observed during the present research. The paper details that fracture, in tests conducted using the wide support configuration, initiates at the outer edge of the flange-skin interface and propagates inward to the specimen’s center, rather than originating from the resin rich region in the center of the specimen and extending outward. This prying type of delamination is described as an asymmetric DCB specimen with a point load acting at the end of the longer leg. In specimens tested using the narrow support configuration delamination initiated and propagated similarly to what was



illustrated in Chapter III. In all of the Rugg tests ultimate failure occurred due to failure of the skin laminate after the delamination propagated through less than half of the z-pin region.

In (25), mention is made that tests were stopped often to measure crack propagation, but no mention is made of asymmetric propagation in either support width configuration. Because of the complexity and lack of symmetry involved in crack propagation in T-section specimens tested in this report, it is currently not possible to follow crack propagation and make any consistent prediction on the COD or load at which each z-pin row fails.

Despite the differences, Rugg reported similar increases in ultimate strength over un-reinforced specimens when using the wide support configuration: a 40% increase in ultimate load for t-section specimens reinforced with 0.022” diameter pins at a 2% areal/volume density with “modest additional strengthening on progressing to 4% areal/volume density”.

#### Data Scatter.

In Figures 57 and 60, the reader will notice that test data taken from specimens utilizing a 0.022” diameter pin contains a noticeably larger scatter than is seen in that of specimens reinforced with 0.011” diameter pins. Data scatter is important in terms of modeling the reinforced laminates behavior and is dependent primarily on the actual pin density.

As the actual pin density drops, more space exists between adjacent pins and pin rows. Since the load drop associated with each pin row failure is dependent upon the inter-row spacing, specimens with lower actual pin densities have larger load-drops causing the test data to appear more discontinuous and scattered. Conversely, higher actual pin densities result in more continuous properties within the z-pin region as the discreteness of the reinforcement is reduced.

A separate phenomenon that is a consequence of increased inter-row spacing and which causes a significant amount of data scatter is the simultaneous failure of adjacent z-pin rows. Simultaneous row failure occurs, as shown in Figures 61 when the remaining momentum from a pin row failure is more than the subsequent row or rows can withstand. Z-pinning is a discrete reinforcement, thus the local environment surrounding each pin and pin row is different. Variations in the fiber fraction, matrix fraction, insertion angle, insertion depth, fiber breakage, pin breakage and the pin-matrix bond strength can each have a significant effect on a pin's failure strength. As the actual pin density increases, there are enough pins a given pin row to maintain a consistent statistical average and minimize the effects of these variations, thus the overall strength appears more consistent.

## **Performance of DYNA3D Model**

The process dictated in this report of modeling discrete z-pins with continuous smeared fracture properties has shown to be a viable option to closely approximate the mode I failure response of reinforced DCB specimens, although the model is not capable of capturing all the particular details from the test.

Test simulations consistently predicted load and COD values within 5% of the test data for each DCB specimen along the linear region up to peak load and first row failure and slightly exaggerated loads within the propagation region beginning after first row failure. Comparisons of the simulation and experimental data indicate that deviations between the simulation and experimental curves occur at and are compounded by each row failure. When a z-pin row fails the associated drop in load shifts the curve downward below the simulation curve, each successive row failure causes further separation between the curves until the end of the tests where the gap is reduced. Multiple row failures, common in specimens with small pin densities, can therefore cause large deviations between the curves that propagate throughout the duration of the test. Therefore deviations are unavoidable, as they are a consequence of attempting to model a discrete reinforcement with continuous properties, but may be minimized by reinforcing with smaller pins and with higher areal pin densities since as the reinforcement becomes less discrete it more closely matches the continuous model.

## **Future Discussions**

While previous research has determined that z-pinning reduces the elastic modulus of the laminate, the reduction predicted in the process of curve-fitting the data to extract fracture properties is much too high. Future work is planned by ASRI to determine the alteration of in-plane properties by z-pins in various densities. It is expected that these tests will result in modulus reductions similar to the 7-10% reduction found by Steeves and Fleck. If so, the equations used to curve-fit the experimental data should be altered if possible to fall in line with the experimental results.

ENF testing was unable to produce fracture properties because of the unexpected laminate fractures. As evidenced in the research, several specimen geometries exist for testing the mode II response other than the 3-point bend ENF test. While good success has been found with these alternative geometries, it is recommended that future z-pinned mode II testing continue using the ENF specimen geometry because of the amount of work that was been done to create the ENF models. While the reinforced ENF model could not be tested in this research project, the un-reinforced ENF model has produced accurate results throughout the test. Clearly, however, changes must be made to avoid this type of fracture in the future.

Because of the complex failure process involved in T-section specimens, work must to be done to characterize the process before the model can hope to have any utility. Further t-section specimen testing should attempt to incorporate the work of Rugg et. al. as much of the numerical results are derived from beam theory and would likely lend themselves well for use in the type of model used in this analysis. Further, more work must be done to understand the crack propagation trends in t-section specimens.

The inability of the current model to capture the load drops that occur after each pin row failure is an important shortcoming of this modeling technique. However the computational expense that is saved by not tracking such a large number of factors makes this approach worthwhile. Specimens with high actual pin densities have properties which are more predictable, easier to model more amenable to critical applications, but in practical applications structures reinforced with z-pins will have various sizes and densities of reinforcement and will be subject to many loading conditions. Therefore more testing is needed to determine the effectiveness of this modeling technique in the various loading conditions and size configurations.

Future work planned by ASRI includes expanding the present work to 1% and 0.5% pin densities to gain a further understanding of the effect of z-pinning and the further develop the modeling process dictated here in hopes of one day

making it a predictive model. ASRI is further working on impact load test in the T-section and DCB specimen geometries to determine the effect of strain rates much higher than those defined in Chapter III. ASRI is also currently attempting to develop models capable of modeling individual z-pins in hopes of gaining better accuracy and capturing all the details of each test.

## **Conclusion**

The idea of adding fibers to a composite laminate in the thickness direction is a relatively young one, but since z-pinning was introduced a substantial amount of research has been done to understand the response these fibers impart. The present research provided further validation to the idea that z-pinning is an effective means of increasing the fracture toughness of continuous fiber reinforced polymer matrix composites by resisting the progression of delamination.

The amount of research conducted on the subject of z-pinning, is evidence that there is value in understanding how through-thickness reinforcement can improve the fracture properties of composite laminates and from the results of the research it is clear that z-pinning is an effective means of improving delamination resistance. Industry has shown that achieving the goal of an all-composite aerospace design is immensely worthwhile, in terms of both cost and performance. Thus it is imperative that technologies, that may hold the keys to overcoming the current survivability obstacles and reaching this goal, be fully explored.

## Bibliography

1. United States Code, Title 10, Section 2366, Live Fire Law
2. Committee on the Study of Live Fire Survivability Testing of the F-22 Aircraft, Commission on Engineering and Technical Systems, National Research Council, *Live Fire Testing of the F-22*, National Academy Press, 1995 ISBN 0-309-05333-1
3. Childress, J., *Decoupled Fuel Cells, Survivability and Manufacturing Demonstration Final Report*, Boeing Report D950-10425-1, 1999
4. Department of the Air Force, *SBIR Phase I Award Selections (with abstracts) Volume III*, 1994, Topic # 94-150
5. Department of the Navy, *SBIR Phase I Award Selections (with abstracts) Volume II*, 1994, Topic # 93-281
6. Methods Development Groups, LLNL, *DYNA3D: A Nonlinear, Explicit, Three-Dimensional Finite Element Code for Solid and Structural Mechanics – User Manual*, Jerry I. Lin - Current Developer 2004
7. Jain L-K, Mai Y-W, *On the Effect of Stitching on Mode I Delamination Toughness of Laminated Composites*, Composites Science and Technology, Vol. 51, pp 331-345, 1994
8. Dai S-C, Liu H-Y, Yan W., Mai Y-W, *Experimental Study of Z-Pin Bridging Law by Pullout Test*, Composites Science and Technology, Vol. 64, pp 2451-2457, 2004
9. Grassi, M. and Zhang, X., *Finite Element Analyses of Mode I Interlaminar Delamination in Z-Fibre Reinforced Composite Laminates*, Composites Science and Technology, Vol. 63, pp. 1815-1832, 2003
10. Zhang, X., Liu H-Y, Mai Y-W, Diao, X-X, *On Steady State Fiber Pull-out II: Computer Simulation*, Composites Science and Technology, Vol. 59, pp. 2179-2189, 1999

11. Cartie, D. D. R., Troulis, M., Partridge, I. K., *Delamination of Z-pinned Carbon Fibre Reinforced Laminates*, Composites Science and Technology, Vol. 66, pp. 855-861, 2006
12. Zhang, X., Liu H-Y, Mai Y-W, Diao, X-X, *On Steady State Fiber Pull-out I: The Stress Field*, Composites Science and Technology, Vol. 59, pp. 2179-2189, 1999
13. Liu, H-Y, Mai, Y-W, *Effect of Z-pin Reinforcement on Interlaminar Mode I Delamination*, Proceeding of the 13<sup>th</sup> International Conference on Composite Materials, ICCM13, Beijing, China, 2001
14. Dugdale, D. S., *Yielding of Steel Sheets Containing Slits*, Journal of Mechanics and Physics of Solids, Vol. 8, pp. 100-104, 1960
15. Barenblatt, G. I., *The Mathematical Theory of Equilibrium Cracks in Brittle Fracture*, Advances in Applied Mechanics, Academic Press, New York, 1962
16. Geubelle, P. H., Baylor, J. S., *Impact-Induced Delamination of Composites: a 2D Simulation*, Composites, Vol. 29-B, pp. 589-602, 1998
17. Paulino, G. H., Zhang, Z., *Cohesive Zone Modeling of Dynamic Crack Propagation in Functionally Graded Materials*, Proceeding of 5<sup>th</sup> GRACM – International Congress on Computational Mechanics, Limassol, Cyprus 2005
18. Borg, R., Larsgunnar N., and Simonsson K., *Modeling of Delamination Using a Discretized Cohesive Zone and Damage Formulation*, Composites Science and Technology, Vol. 62, pp. 1299-1314, 2002
19. Reedy, E. D., Mello, F. J., Guess, R. R., *Modeling of the Initiation and Growth of Delamination in Composite Structures*, Journal of Composite Materials, Vol. 31, pp. 812-831, 1997
20. Xu, X. and Needleman, A., *Numerical Simulation of Fast Crack Growth in Brittle Solids*, Journal of Mechanics and Physics of Solids, Vol. 42, pp. 1397-1434, 1994



21. Steeves, C. A., Fleck N. A., *In-Plane Properties of Composite Laminates with Through-Thickness Pin Reinforcement*, Cambridge University Engineering Department, 2005  
Website: <http://www.mech.eng.cam.ac.uk/profiles/fleck/papers/204.pdf>
22. Yan, W., Liu, H-Y, Mai, Y-W, *Mode II Delamination Toughness of Z-pinned Laminates*, Composites Science and Technology, Vol. 64, pp. 1937-1945, 2004
23. Cartie, D. D. R., Cox, B. N., Fleck, N. A., *Mechanisms of Crack Bridging by Composite and Metallic Rods*, Composites: Part A: Applied Science and Manufacturing, Vol. 35, pp. 1325-1336, 2004
24. Grassi, M., Zhang, X., Meo, M., *Prediction of Stiffness and Stresses in Z-fiber Reinforced Composite Laminates*, Composites Part A: Applied Science and Manufacturing, Vol. 33, pp. 1653-1664, 2002
25. Rugg, K.L., Cox, B.N., Massabo, R. *Mixed mode delamination of polymer composite laminates reinforced through the thickness by z-fibers*, Composites, Part A: applied science and manufacturing, Vol. 33, pp 177-190, 2002

<b>REPORT DOCUMENTATION PAGE</b>				<i>Form Approved OMB No. 074-0188</i>	
<p>The public reporting burden for this collection of information is estimated to average 1 hour per response, including the time for reviewing instructions, searching existing data sources, gathering and maintaining the data needed, and completing and reviewing the collection of information. Send comments regarding this burden estimate or any other aspect of the collection of information, including suggestions for reducing this burden to Department of Defense, Washington Headquarters Services, Directorate for Information Operations and Reports (0704-0188), 1215 Jefferson Davis Highway, Suite 1204, Arlington, VA 22202-4302. Respondents should be aware that notwithstanding any other provision of law, no person shall be subject to a penalty for failing to comply with a collection of information if it does not display a currently valid OMB control number.</p> <p><b>PLEASE DO NOT RETURN YOUR FORM TO THE ABOVE ADDRESS.</b></p>					
<b>1. REPORT DATE (DD-MM-YYYY)</b> 14 Sep 2006		<b>2. REPORT TYPE</b> Master's Thesis		<b>3. DATES COVERED (From - To)</b> Aug 05 - Sep 06	
<b>4. TITLE AND SUBTITLE</b>  <b>Modeling Fracture in Z-Pinned Composite Co-Cured Laminates Using Smeared Properties and Cohesive Elements in DYNA3D</b>				<b>5a. CONTRACT NUMBER</b>	
				<b>5b. GRANT NUMBER</b>	
				<b>5c. PROGRAM ELEMENT NUMBER</b>	
<b>6. AUTHOR(S)</b>  Freels, Jason, K., Captain, USAF				<b>5d. PROJECT NUMBER</b> ENR #	
				<b>5e. TASK NUMBER</b>	
				<b>5f. WORK UNIT NUMBER</b>	
<b>7. PERFORMING ORGANIZATION NAMES(S) AND ADDRESS(S)</b> Air Force Institute of Technology Graduate School of Engineering and Management (AFIT/EN) 2950 Hobson Way WPAFB OH 45433-7765				<b>8. PERFORMING ORGANIZATION REPORT NUMBER</b>  AFIT/GMS/ENY/06-S01	
<b>9. SPONSORING/MONITORING AGENCY NAME(S) AND ADDRESS(ES)</b> AFRL/MLBC Attn: Dr. Richard Hall Bldg 643 Hobson Way WPAFB OH 45433  DSN: 785-9097				<b>10. SPONSOR/MONITOR'S ACRONYM(S)</b>	
				<b>11. SPONSOR/MONITOR'S REPORT NUMBER(S)</b>	
<b>12. DISTRIBUTION/AVAILABILITY STATEMENT</b> APPROVED FOR PUBLIC RELEASE; DISTRIBUTION UNLIMITED.					
<b>13. SUPPLEMENTARY NOTES</b>					
<b>14. ABSTRACT</b> The purpose of the present research was three-fold: 1) gain a more sophisticated understanding of the response of co-cured composite joints with and without through-thickness reinforcement (TR), 2) compare the behavior of specimens reinforced with various sizes and densities of reinforcement, and 3) use experimental data to verify the existing DYNA3D smeared property model. Double cantilever beam, end-notch flexure and T-section specimens reinforced with 0.011" diameter z-pins at 2% and 4% volume densities were tested to determine the mode I, mode II and mixed mode (I and II) behavior. Results were added to preliminary research in which tests were conducted on previously mentioned specimen geometries reinforced with 0.022" diameter z-pins at similar densities. Experiments were modeled in DYNA3D using shell and cohesive elements. The energy release rate, $G$ , determined through a curve fit developed from beam theory, was smeared across the region of reinforcement treating it as a separate material. The research validated Z-pinning as an effective means of improving the fracture toughness of polymer matrix laminated composites in mode I and mixed mode loading conditions and determined that the existing model works well in simulating the behavior in mode I tests.					
<b>15. SUBJECT TERMS</b> Z-pins, Through-Thickness Reinforcement, Composites, Cohesive Modeling,					
<b>16. SECURITY CLASSIFICATION OF:</b>			<b>17. LIMITATION OF ABSTRACT</b>  UU	<b>18. NUMBER OF PAGES</b>  105	<b>19a. NAME OF RESPONSIBLE PERSON</b> Dr. Som Soni
REPORT U	ABSTRACT U	c. THIS PAGE U			<b>19b. TELEPHONE NUMBER (Include area code)</b> (937) 255-3636, ext 3420; som.soni@afit.edu

**Standard Form 298 (Rev. 8-98)**  
Prescribed by ANSI Std. Z39-18